

# The eclipsing binary V578 Mon in the Rosette nebula: age and distance to NGC 2244 using Fourier disentangled component spectra<sup>\*,\*\*</sup>

H. Hensberge<sup>1</sup>, K. Pavlovski<sup>2</sup>, and W. Verschueren<sup>3,\*\*\*</sup>

<sup>1</sup> Royal Observatory of Belgium, Ringlaan 3, 1180 Brussel, Belgium

<sup>2</sup> University of Zagreb, Faculty of Geodesy, Kačićeva 26, 10000 Zagreb, Croatia

<sup>3</sup> University of Antwerp (RUCA), Astrophysics Research Group, Groenenborgerlaan 171, 2020 Antwerpen, Belgium

Received 8 December 1999 / Accepted 10 April 2000

**Abstract.** V578 Mon is a member of the young stellar cluster NGC 2244 which is embedded in the Rosette nebula. It is a double-lined binary, consisting of two early-B type components which eclipse each other partially during their 2.40848-day orbit. A novel technique of Fourier disentangling is applied to disentangle the spectrum of the binary into the spectra of its components, allowing a direct spectroscopic temperature determination for each component. Together with an analysis of the light curve, the spectral disentangling process allows us to derive the orbital and fundamental stellar parameters. The hotter star ( $T_{\text{eff}} = 30\,000$  K) has a mass of  $14.5 M_{\odot}$  and a radius of  $5.2 R_{\odot}$ . The cooler one ( $T_{\text{eff}} = 26\,400$  K) has a mass of  $10.3 M_{\odot}$  and a radius of  $4.3 R_{\odot}$ . Both stars are well inside their critical Roche lobe and move in an eccentric orbit ( $e=0.087$ ) which has a semi-major axis of  $22 R_{\odot}$  and is seen at an inclination of  $72.6^{\circ}$ . The rotation of both stars is synchronized with the orbital motion. The systemic velocity of  $34.9 \text{ km s}^{-1}$  confirms that the binary belongs to NGC 2244. The age of the binary, and hence of NGC 2244, is  $(2.3 \pm 0.2) 10^6$  years. From the fundamental stellar parameters and the interstellar absorption, the distance to the cluster is derived to be  $1.39 \pm 0.1$  kpc, i.e. slightly lower than that found from photometric studies. Its age and space velocity indicate that NGC 2244 is formed in the galactic plane. The high accuracy obtained (e.g. probable errors of 0.5% for the masses, 1–1.5% for the radii, despite the lack of total eclipses, and 1.5% for the temperatures) is a direct consequence of the spectral disentangling technique, which as a by-product delivers very accurate radial velocities for all orbital phases.

**Key words:** techniques: radial velocities – stars: binaries: eclipsing – stars: distances – stars: individual: V578 Mon (HDE 259 135) – stars: fundamental parameters – Galaxy: open clusters and associations: individual: NGC 2244

Send offprint requests to: H. Hensberge (herman@oma.be)

\* Based on observations obtained at the European Southern Observatory (ESO), La Silla, Chile

\*\* Table 5 is only available in electronic form at the CDS via anonymous ftp to 130.79.128.5 or at <http://cdsweb.u-strasbg.fr>

\*\*\* Postdoctoral Fellow of the Fund for Scientific Research – Flanders (Belgium) (F.W.O.)

## 1. Introduction

Eclipsing binary stars in stellar groups are especially interesting. They not only offer the most accurate fundamental stellar data, but also allow one to evaluate characteristics of the group as a whole, like its age and distance, in an independent and precise way. When using fundamental stellar parameters for a distance determination, the most important source of error lies in the bolometric luminosities, and hence a precise determination of stellar temperature and radius is essential. The age determination for main sequence stars by comparison to stellar evolution computations requires an accurate gravity estimate which must be derived from the masses and the radii. Double-lined eclipsing binaries are the most precise source for masses and radii, and novel spectral disentangling techniques now offer the possibility to estimate the temperatures of the components spectroscopically with the same precision as for single stars.

This prompted us to make a detailed analysis of the double-lined eclipsing binary V578 Mon (HDE 259135  $\equiv$  BD+4°1299) which is a member of the young stellar cluster NGC 2244 (e.g. Marschall et al. 1982). NGC 2244 (C0629+049) is itself embedded in the famous Rosette Nebula (NGC 2237 - NGC 2246) and is situated inside the older Mon OB2 association. The expanding ionization front generated by its massive OB stars has in its turn triggered new star formation in the dense regions of the Nebula (see e.g. Cox et al. 1990). Modern photometric studies place NGC 2244 at a distance of 1.4 to 1.7 kpc, depending on luminosity calibrations and extinction assumptions, but contamination by binaries must also be important. An overview of the large-scale structures in Northern Monoceros can be found in Pérez (1991).

V578 Mon is composed of two early-B main-sequence stars. Not many massive systems have been well-analyzed at present. In a critical review, Harries & Hilditch (1998) have recently compiled a list that contains only 8 eclipsing systems with components earlier than B0.5 V. Fundamental data for more systems are thus welcome for a critical comparison with stellar models. In this paper, the spectra of the two components of V578 Mon are separated by application of a novel technique of Fourier disentangling. From the component spectra, spectroscopic temperatures (and other atmospheric parameters) can be derived

straightforwardly as in the case of single stars. That avoids the use of statistically valid temperature vs. colour or temperature vs. spectral type relations in order to compensate for the fact that the analysis of light and radial velocity variations fixes only the ratio of the temperatures of the components. The disentangling provides, as a by-product, precise radial velocities at all phases and thus circumvents the classical problem of measuring the position of lines consisting of highly blended components arising in the two stars. Together with the light curves, these radial velocities allow one to obtain improved dynamical parameters in general and the masses and radii in particular.

First, the method of analysis applied in this paper is described (Sect. 2). In Sect. 3, a short review of previous observations of V578 Mon is given, followed by the description of the spectroscopy and photometry presented here (Sect. 4) and the orbital period derived from them (Sect. 5). Sect. 6 forms the main part of the paper. It contains the details of the different analyses (spectral disentangling, light- and radial-velocity variations, spectroscopic analysis of the individual components) and the resulting orbital and fundamental stellar parameters. The implications of these results for NGC 2244 are summarized in Sect. 7. A discussion of these results and the general conclusions are presented in Sect. 8. In this paper, the stars in NGC 2244 are referred to by the identification numbers introduced by Ogura & Ishida (1981), except for the eclipsing binary (#200 in their system) for which its variable star name V578 Mon is used throughout. With the first reference to a given star, we also give its HD or HDE identification and the number assigned by Johnson (1962) preceded by the letter J ( $J8 = V578 \text{ Mon}$ ).

## 2. Analysis method

### 2.1. General procedure

The combination of different analysis tools to analyse the signatures of the orbital movement and the component spectra may lead to a more precise and complete picture of an eclipsing binary system. It is well-known that some parameters, or combinations of them, are strongly constrained by the light variations (e.g. radii in units of the orbital semimajor axis  $A$ ; the latter is determined by the spectroscopic orbit), and others rather by the changes in radial velocity (e.g. masses, when combined with the inclination  $i$  of the orbital plane as derived from the light variations). Only the ratio of the stellar temperatures can be constrained by the light variations; both temperatures are best derived from the analysis of each of the individual components separately, as one would do for single stars. This is possible after applying spectral disentangling techniques as first developed by Simon & Sturm (1992, 1994) and independently by Hadrava (1995).

The tools used to extract the radial velocities and to derive the orbital and stellar characteristics depend on each other. Each of them may benefit from information provided by the others, and thus an iterative loop is needed. Fig. 1 sketches the three main structures of such a loop, and their inter-relations. The classical core is the model used to analyse the variations in light and radial velocity caused by the orbital motion (upper oval

in Fig. 1). While the light variability is measured straightforwardly, radial velocities may be more difficult to obtain from the composite spectra, especially at orbital phases when the differences between the velocities of the components are small. The lack of (precise) velocities at those phases is reflected in the uncertainties in eccentricity and periastron longitude. However, methods developed to disentangle the component spectra also provide precise radial velocities. Those form the second basic tool (lower oval in Fig. 1) in the analysis. The component spectra may then be analyzed as in the case of single stars using stellar atmosphere models. These models form the third cornerstone (middle oval in Fig. 1) of the analysis.

With these three cornerstones at hand, parameter estimation can gain in robustness when information that may be derived with higher accuracy using one specific tool is allowed to constrain the fitting process in another tool: e.g. in the analysis of the component spectra, the temperatures may be better constrained than in the case of single stars because the gravities are known accurately from the dynamically derived masses and radii. An overview of the most obvious interactions between the cornerstones which permit a gain in robustness is sketched in Fig. 1. As a starting point, the spectrum disentangling could be applied keeping the component light ratio in each spectrum as a free parameter, to obtain radial velocities (case 1). Alternatively, radial velocities of selected lines could be measured in a classical way (maybe only in some orbital phases) and combined with the light-curve(s) to obtain an initial orbital solution including the wavelength-dependent light ratio between the components (case 2). Which strategy is best will depend on the specific system, especially on the component light ratio and the complexity of the spectrum, but also on the accuracy of photometry and spectroscopy and on the effort needed to obtain a converging solution. In either case, the complementary tool is used immediately thereafter with either better radial velocities as input (case 1) or better light ratios that may be fixed for each of the spectra during the spectral disentangling (case 2). If the iterated solution leads to a significant change in the input parameters for the complementary tool, then additional iterations must be performed.

The spectral disentangling tool delivers the contribution of the component spectra with a normalisation that is linked to the normalisation of the composite spectrum. The component spectra should be renormalized using the wavelength-dependent light ratio provided by the light-curve analysis. A stellar-atmosphere analysis, constrained by the dynamical gravities and the orbital inclination angle, provides then the effective temperatures, the rotational velocities and any more detailed information on abundances, macroscopic and microscopic broadening etc. To a first order, the information flow appears to be directed from the two tools for the dynamical analysis to the atmosphere analysis as indicated in Fig. 1 and not in the reverse direction. However, practice suggests strongly that the analysis of the intrinsic component spectra might be used in some cases to improve the disentangling of the composite spectra. Wrong initial normalisations or the presence of spectral components that do not participate in the Doppler shifts of the component spec-

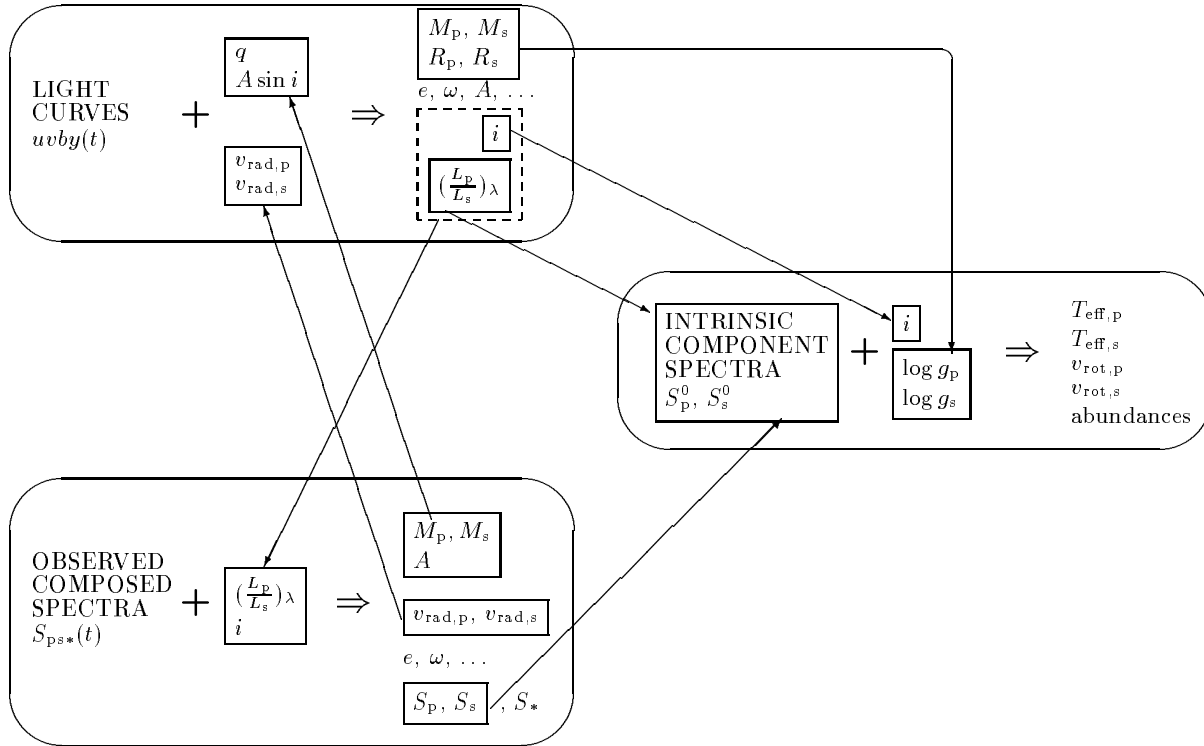


**Fig. 1.** Input-output interaction between the different types of analysis tools. The structure in each oval represents the scheme ‘data + indirect input  $\Rightarrow$  output parameters’, with allowance for the fact that the ‘indirect input’ is best obtained after application of the tool from where the arrow starts. The output parameters mentioned in each oval take into account this indirect input; in the initial iteration, the output is more restricted, as can be found in any textbook on eclipsing binaries. The subscripts p and s refer to the two stars, the \* subscript stands for all other components that might contribute (e.g. interstellar, circumstellar, terrestrial lines). The superscript 0 for the intrinsic component spectra indicates that they are normalized to their own continua rather than to the observed combined one. All other symbols have their standard meaning, and are explained in, and used throughout, the text.

tra, e.g. features of interstellar or circumstellar origin, generating enhanced, spurious features after re-normalisation, which stand out most clearly in the spectrum of the less bright component. This back-coupling is not yet exploited in the present paper, but is necessary in a spectral fine analysis that relies on weak(er) lines in some spectral regions. The specific iteration scheme applied in this paper is presented in Sect. 6, after the description of the available data and their quality.

## 2.2. Tools

In this paper, the concept outlined in Sect. 2.1 is followed using FOTEL (Hadrava 1990) and the Wilson-Devinney WD programme (Wilson 1979) for the simultaneous analysis of the light and the radial velocity variations, KOREL (Hadrava 1995) for the spectral disentangling, and line-blanketed LTE models of Kurucz (1992) for solar abundances, with depth-dependent non-LTE line formation computations using the DETAIL and SURFACE programmes (Giddings 1981, Butler & Giddings 1985) for the analysis of the component spectra. SURFACE solves the transfer equation using the results of detailed broadening calculation based on the *Unified Theory* (Vidal et al. 1974), as worked out by Vidal et al. (1970) for H I, Barnard et al. (1969, 1974) or Bennett & Griem (1971) for He I and Schöning & Butler

(1989a,b) for He II. References for the models of the different chemical elements can be found in the study of early-B stars in NGC 2244 by Vrancken et al. (1997).

The WD programme is a standard tool in binary research, dating back to its original release by Wilson & Devinney (1971), but with substantial improvements by Wilson (1979), who generalized it for eccentric orbits and for simultaneously solving multi-passband photometry and radial velocities. The programme is documented and maintained by Wilson (1992, 1993). We used the version of Sept. 1993 in the differential correction mode starting from a solution obtained with FOTEL, which allows treatment of the light and radial-velocity data in a slightly different way and provides error estimates taking into account the covariance matrix. Each measurement and/or data set can be weighted in a least-squares minimization procedure. FOTEL also solves for offset in zero-points between different data subsets for the same quantity. It can handle eccentric orbits of binary stars including a third companion.

We will give a somewhat more extended introduction to KOREL, since this method of spectral disentangling is not yet widely used. Historically, the low efficiency encountered in measuring radial velocities line by line and, later, the availability of digital spectra lead to the introduction of the cross-correlation technique in which the observed spectrum is compared with tem-

plates which mimic the (expected) spectra of the components (Simkin 1974). However, the choice of an appropriate template (either an observed spectrum of a single star or a synthesized spectrum) is seldom straightforward. The spectral disentangling technique makes the use of a template obsolete.

KOREL assumes that the observed spectrum,  $I(x, t)$  is composed of the *time-independent* intrinsic spectra  $I_j(x)|_{j=1}^n$  of  $n$  stars, each one Doppler shifted according to the instantaneous radial velocity  $v_j(t)$  of the star  $j$  at the time  $t$ . The composite spectrum is given by convolution in  $x = c \ln(\lambda)$ , logarithmic in wavelength:

$$I(x, t) = \sum_{j=1}^n s_j(t) I_j(x) * \delta(x - v_j(t)). \quad (1)$$

The functions  $s_j(t)$  describe an overall change in the relative contribution of a component to the composite spectrum, due to geometric effects in the binary system (ellipticity and/or eclipses). The Fourier transform ( $x \rightarrow y$ ) of this equation reads:

$$\tilde{I}(y, t) = \sum_{j=1}^n s_j(t) \tilde{I}_j(y) \exp(iy v_j(t)). \quad (2)$$

If  $k$  spectra ( $k > n$ ) have been observed at times  $t_i|_{i=1}^k$ , corresponding to various values of  $v_j(t_i)$ , they can – in principle – be fitted by searching for appropriate values of  $v_j(t_i)$ ,  $s_j(t_i)$  and  $\tilde{I}_j(y)$ . Hadrava applies a least-squares fit to the Fourier transform of the observed spectra, which provides an easier numerical solution than the algorithm applied by Simon & Sturm (1994). For further details, the reader is referred to Hadrava (1995, 1997, 1998).

The velocities  $v_j(t_i)$  can be treated either as independent values, or can be given functions of time and certain parameters  $p$ , e.g. the orbital elements of the spectroscopic binary. Moreover, KOREL enables the disentangling of spectra originating from multiple stellar systems with a different hierarchical structure (up to 5 components are allowed). This enables the separation of telluric lines and/or interstellar lines, for example, from the stellar spectra. The version of KOREL we have used can handle simultaneously up to 45 exposures each subdivided into not more than 5 spectral regions, though the number of spectral regions times the number of components should not exceed 15; each spectral region may contain at most 1024 logarithmic wavelength bins.

In summary, spectral disentangling looks for a self-consistent solution of orbital elements, Doppler shifts, component spectra and component relative intensities. In some sense, it is a combination of the cross-correlation technique (measuring radial velocities, but without the need for a pre-defined template) and the Doppler tomography (Bagnuolo & Gies 1991), the latter also separating the component spectra but using pre-defined radial velocities.

### 3. An observational history of V578 Mon

The observational history on V578 Mon is by no means rich, although it was noted long ago as a radial-velocity and light

variable, and even as a double-lined binary. The first radial velocity measurements of HDE 259135 ( $v_{\text{rad}} = -80 \text{ km s}^{-1}$  and  $+48 \text{ km s}^{-1}$  at 2 different epochs) date from the late twenties (Hayford 1932) and indicate that it is a spectroscopic binary. They were obtained at Lick Observatory in the framework of an extensive observational programme in open clusters. Apparently, that was overlooked later on, since Sanford (1949) includes his single measurement of  $+12 \text{ km s}^{-1}$  in the distance and radial-velocity determination for NGC 2244.

The first photometric studies of the cluster (Hiltner 1956, Johnson 1962) did not notice the light variability, although in particular Johnson (1962) assigns variability to 3 other stars. His paper also presents the B0 V classification by W. W. Morgan. Later, Morgan et al. (1965) published more accurate spectral types for the brighter stars in NGC 2244 and NGC 2264, based on classification spectrograms obtained at the 82-inch reflector of the McDonald Observatory. HDE 259135 (=V578 Mon) was noted explicitly by them as a double-lined binary of spectral type B0.5 V.

The first publication of the star's photometric variability goes back to Heiser's (1977) thorough *uvby* $\beta$  study of NGC 2244. He followed-up the star for several years with photoelectric photometry at Dyer Observatory. It is interesting to note that the star bears its variable star designation, V578 Mon, through Heiser's (1971) annual observatory report, in spite of the fact that no photometric data or light curves were published. The next Dyer Observatory annual report (Heiser 1972) also mentions a set of medium-resolution spectra obtained at KPNO, which yielded approximately equal radial-velocity amplitudes of about  $350 \text{ km s}^{-1}$  for both components. The orbital period was noted to be 2.420 d and to fit both their photometric and spectroscopic data.

## 4. Observations and data reduction

### 4.1. Echelle spectroscopy

In January/February 1993 echelle spectra in the wavelength range 3600–5000 Å were obtained with CASPEC mounted in Cassegrain mode at the 3.6 m telescope of ESO at La Silla. We came to an agreement with Blaauw and Sahu that we should combine our respective short observing runs; an arrangement that was essential for obtaining an acceptable coverage of orbital phases in 7 nights. CASPEC was used with the 52 grooves/mm echelle grating and the 300 grooves/mm cross-dispersing grating blazed at 4230 Å, in combination with a 1."4 wide slit (rotated to the parallactic angle) and CCD #32, a thinned and anti-reflection coated Tektronix CCD with 512 x 512 27  $\mu$  pixels. Spectra with a signal-to-noise ratio ( $S/N$ ) > 100 longward of 4000 Å were typically obtained in 20 minutes. In 3 cases, an exposure was repeated to increase the  $S/N$ . Some spectra taken at higher air mass are noisy below 4000 Å (Fig. 2). Thorium-Argon lamp and Tungsten lamp spectra were obtained with each observation. An observing log is given in Table 1.

The data reduction procedure applied follows closely the one presented in Verschueren et al. (1997), resulting in spectra binned in  $\ln \lambda$  with steps corresponding to  $8.2 \text{ km s}^{-1}$  in ve-

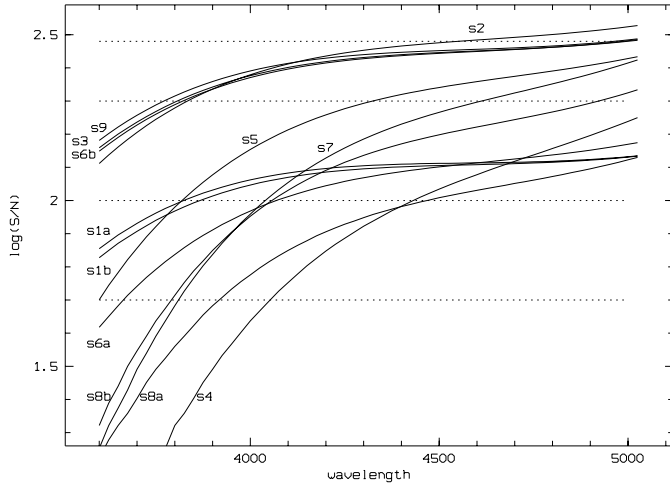


**Fig. 2.**  $S/N$  ratio for all spectra of V578 Mon as derived from the propagation of read-out noise and photon shot noise in the data reduction process. Dashed horizontal lines indicate a  $S/N = 50, 100, 200, 300$ .

**Table 1.** Observation log of the spectroscopy. Heliocentric Julian dates (HJD) are given for mid-exposure time. Orbital phases are computed using the ephemeris given in Sect. 5. The fourth column gives the exposure time, the sixth the heliocentric velocity correction that was applied to the spectrum.

HJD	spec. ident.	phase	exp. [s]	airmass	HVC [km s <sup>-1</sup> ]
2 400 000+					
49018.6136	s1a	-0.005	780	1.21	-15.40
49018.6259	s1b	0.000	720	1.21	-15.44
49019.5729	s2	0.393	1080	1.24	-15.70
49020.6317	s3	-0.167	900	1.23	-16.30
49020.7663	s4*	-0.111	1500	2.39	-16.62
49021.7329	s5	0.290	1200	1.81	-16.97
49022.5723	s6a	-0.362	960	1.23	-16.95
49022.5904	s6b	-0.354	960	1.21	-17.00
49022.7656	s7	-0.281	1800	2.53	-17.44
49023.7275	s8a	0.118	1200	1.81	-17.77
49023.7475	s8b	0.126	1200	2.14	-17.81
49024.5710	s9	0.468	1200	1.22	-17.75

\* Slit EW

locity. Rather than rectify all the spectra independently, we first related the flux level  $F_i(m, \lambda)$  in each spectral order  $m$  of each spectrum  $i$  to that of the reference spectrum s3 (Table 1):

$$F_{s3}(m, \lambda) = f_i(m, \lambda)F_i(m, \lambda) \quad (3)$$

The functions  $f_i$  were derived from selected spectral regions such that the influence of the Doppler shifts of strong spectral features is negligible. The fact that one of the spectral orders, centered around 4790 Å, is almost free of spectral lines allowed us to derive the slope of  $f_i$  in that order in an empirical way. In other orders, the change in shape of  $f_i$  was obtained through a low-order bivariate polynomial that imposed the required smoothness. The change of shape in  $f_i$  is dominated by the variation of slit losses in different exposures, but second-order changes in atmospheric extinction (the influence of ‘standard’

**Table 2.** Photometry of *wby* standard stars and local standards reduced to the standard system.

HR	$N_{\text{obs}}$	$V_j$	$b - y$	$m_1$	$c_1$
2056	7	4.869 <sup>1</sup>	-0.066	+0.105	+0.416
2106	7	4.368	-0.070	+0.087	+0.366
2707	7	5.430 <sup>2</sup>	+0.184	+0.178	+0.872
2880	7	5.248	+0.127	+0.170	+1.195
2927	7	5.137	+0.282	+0.175	+0.647
2961	6	4.842	-0.079	+0.098	+0.305
3084	7	4.510 <sup>3</sup>	-0.078	+0.097	+0.253
3314	7	3.902	-0.014	+0.164	+1.023
3410	7	4.147	+0.005	+0.153	+1.092
3454	6	4.299	-0.082	+0.090	+0.238
3849	7	5.070	-0.063	+0.103	+0.412
4119	7	5.075	-0.056	+0.106	+0.483
4293	6	4.417 <sup>4</sup>	+0.055	+0.186	+1.117
4343	4	4.463	+0.009	+0.165	+1.194
4515	7	4.849	+0.088	+0.200	+0.916
2244-#114*	6	7.599	+0.206	-0.040	-0.081
2244-#122*	9	6.756	+0.166	-0.011	-0.114
2244-#203*	8	7.273	+0.232	-0.031	-0.119

\* Ogura & Ishida (1981) identification numbers in NGC 2244

<sup>1</sup> light variable, rms( $V_j$ ) = 0.015 mag;

<sup>2</sup> light variable, rms( $V_j$ ) = 0.011 mmag;

<sup>3</sup> light variable, rms( $V_j$ ) = 0.021 mag;

<sup>4</sup> light variable? (0.03 mag fainter than predicted)

extinction at the respective airmasses was removed earlier), and instrumental factors also contribute. The order of magnitude of the changes due to instrumental factors can be evaluated from flat-field exposures. Finally, the blaze profile determination and the merging of the spectral orders is applied identically to the reference spectrum s3 and all transformed spectra  $f_i F_i$ . In that way, differential continuum placement errors, obviously one of the limiting factors in disentangling the component spectra, are kept low.

#### 4.2. *wby* photometry

In January 1994 the light-curve was obtained during a 12-night run at the SAT 0.5 m telescope at La Silla, equipped with a multi-channel photometer. Differential photometry (Table 5) was obtained relative to the stars # 115 (J5, HD 46106) and # 128 (J10, HDE 259105), which were anticipated to be near in spectral type to the components of V578 Mon. Sky background measurements were obtained 30'' E of V578 Mon, 50'' E of # 115 and 55'' SW of # 128. Light curves (Fig. 3) are presented in the instrumental system. Error bars refer to the rms in the differential observations, derived from the photon shot noise and from the internal scatter in repeated 20-second integrations. The typical 1  $\sigma$  error bar on the final differential magnitudes is 3 millimag. The higher accuracy of the colours is typical for multi-channel photometry. The observations made at the SAT by J. Andersen during 4 nights in 1992, differential to # 115 and # 180 (J6, HD 46202) are added to the light curves.

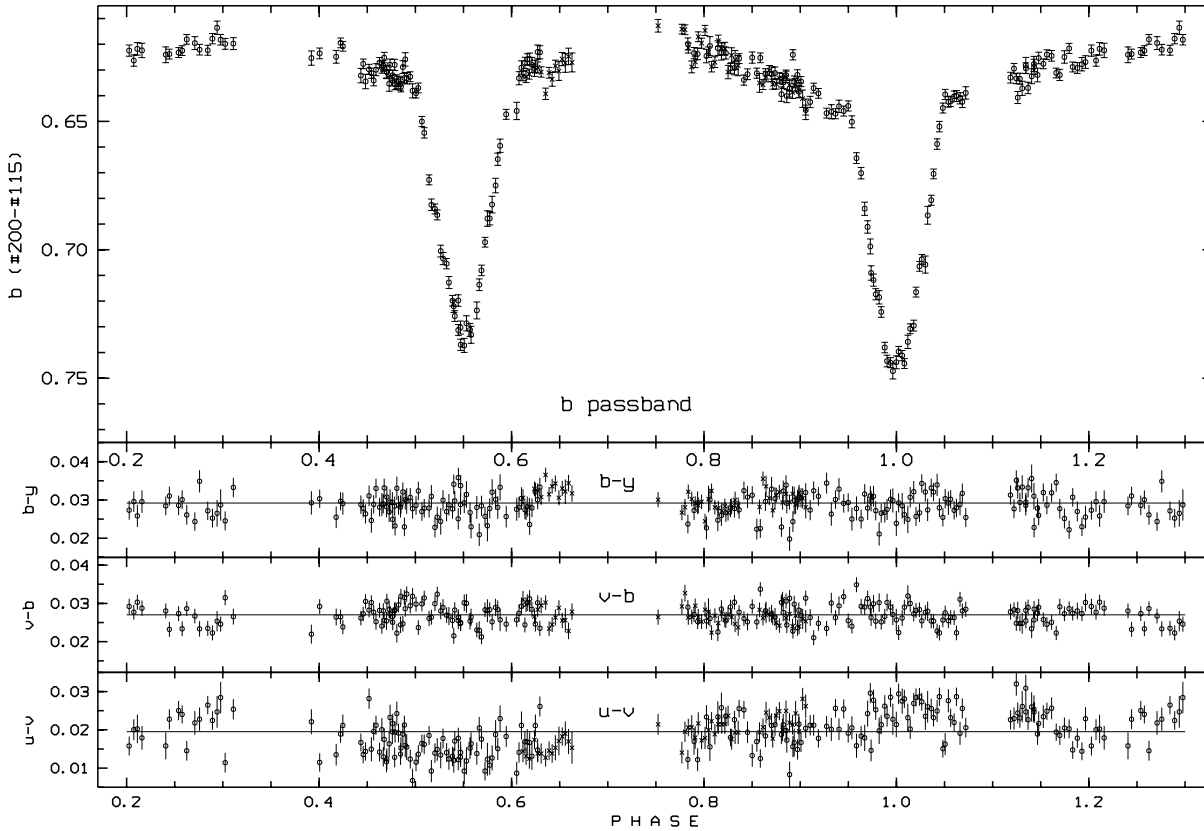


**Fig. 3.** Light curve in Strömgren b and colour variations of V578 Mon, all relative to star # 115, as measured on the SAT by Andersen (crosses) and Hensberge (circles).  $1\sigma$  error bars are computed as explained in the text. Horizontal lines indicate the mean observed differential colour out of eclipses.

Absolute photometry is based on the observation of 15 standards of spectral types B to F from the list of Crawford (1975) and 3 ‘secondary standards’ of spectral type O in NGC 2244. Details are given in the Tables 2 and 3. The transformation equations for the instrumental values, corrected for declination as given in Gray & Olsen (1991), are:

$$V_J = y_i + 0.02(b - y) + \text{constant} \quad (4)$$

$$b - y = 1.013(b - y)_i + 0.180 \quad (5)$$

$$m_1 = 1.000 m_{1i} - 0.004(b - y) - 0.025 \quad (6)$$

$$c_1 = 1.013 c_{1i} + 0.155(b - y) - 0.028 \quad (7)$$

Together with Walraven photometry and  $H_\beta$  photometry from February 1991 obtained earlier by us, and Geneva photometry from P. Lampens obtained in December 1992 and January 1994, the new data describe the colours of the binary in the near-UV and visual (Table 4). All information in that table is derived from out-of-eclipse data; moreover, Fig. 3 shows that colour changes during eclipse are minor.

## 5. Orbital period

From the photometry and the spectroscopy which were obtained with a delay of about one year, it is immediately clear that Heiser’s period of 2.42 days needs to be refined. Using in addition a few spectra taken in January 1992 and December 1993,

it became obvious that the correct period should be in the range  $2.4085 \pm 0.0005$  days. Once this period estimate was obtained, D. Hall (1994) informed us that, adding his and Heiser’s photometry, apsidal motion is detected. He reproduced all times of eclipses with a period of  $2.40848 \pm 0.00001$  days. Hence, we use:

$$\text{HJD}(\text{primary eclipse}) = 2\,449\,360.625 + 2.40848 E \\ \pm 0.001 \quad \pm 0.00001$$

Phase 0.0 was fixed by fitting a parabola simultaneously to the Strömgren *uvby* data over phase intervals of  $\pm 0.02$ – $0.03$ , iteratively centered around the ‘primary’ eclipse. In the presence of apsidal motion the distinction between the eclipses is not always straightforward. The one defined here as ‘primary’ eclipse will be shown later to correspond to the cooler star passing in front of the hotter one.

## 6. The binary V578 Mon

In this section, first a description is given of the iterative procedure as applied in practice (see Sect. 2.1 and Fig. 1 for general considerations). Once the general frame of iterations is defined, we specify in separate sub-sections the technical details and discuss the accuracy of the results obtained by the using the three principal tools (see Sect. 2.2), i.e. spectral disentangling (Sect. 6.1), light curve and radial velocity analysis (Sect. 6.2), and analysis of the component spectra (Sect. 6.3).

**Table 3.** Comparison of the SAT photometry transformed to the standard system with the *wby* standard system and with some large photometric studies at the SAT telescope. Average offset and rms scatter are given for each subset of common stars (2<sup>nd</sup> column), in millimag units. The entry between brackets in the visual magnitude column is computed excluding the light variables (see notes with Table 2). Data for the comparison sets can be found in Crawford (1975), Olsen (1983), Gray & Olsen (1991) and Olsen (1993).

comp. set	nr. stars	$\langle \Delta V_j \rangle \pm \text{rms}$	$\langle \Delta (b - y) \rangle \pm \text{rms}$	$\langle \Delta (m_1) \rangle \pm \text{rms}$	$\langle \Delta (c_1) \rangle \pm \text{rms}$
Crawford STD	18	+0.9±15.5 (+2.7±11.3)	-0.1±5.2	-0.1±6.7	+0.1±6.6
Olsen < 1983	15	+0.8±11.2 (-0.6± 3.0)	+0.6±4.7	-2.9±5.7	+1.1±4.5
Olsen 1985-87	12	+2.2±12.4 (+0.2± 6.1)	+0.4±2.5	+1.1±4.0	+0.2±5.4
Gray&Olsen 1987-88	8	-0.3±18.6 (-1.2± 2.4)	-2.1±2.0	+3.9±3.3	-3.3±7.6
Olsen 1988-91	5	+8.4±19.0 (+1.0± 1.7)	+1.2±2.8	+2.6±4.2	-1.8±7.0

**Table 4.** Visual magnitude, colours and photometric indices for V578 Mon and comparison stars, reduced to the various standard systems. Only photometry out of eclipse is used. The number of contributing observations is indicated between brackets. Note that the Walraven system uses a logarithmic rather than a magnitude scale.

photometry	hjd interval [2 440 000.0 +]	V578 Mon HDE259135	#115 HD46106	#128 HDE259105	#180 HD46202	#201	#203 HD46223
Strömgren	9 360.5-71.8						
$b - y$		+0.209 (105)	+0.180 (117)	+0.192 (64)	+0.210 (74)		
$m_1$		-0.027 (105)	-0.025 (117)	+0.001 (64)	-0.028 (74)		
$c_1$		-0.004 (105)	+0.000 (117)	+0.033 (64)	-0.036 (74)		
$\beta$	8 311.7	+2.628 (1)	+2.613 (1)	+2.642 (1)	+2.612 (1)		
Geneva	8 634.4-36.5 9 043.3-44.4						
$G - B$		1.905 (12)				1.919 (5)	1.845 (9)
$V1 - B$		1.474 (12)				1.490 (5)	1.435 (9)
$B2 - B$		1.536 (12)				1.532 (5)	1.527 (9)
$B1 - B$		0.833 (12)				0.825 (5)	0.833 (9)
$V - B$		0.771 (12)				0.783 (5)	0.726 (9)
$U - B$		0.501 (12)				0.502 (5)	0.419 (9)
Walraven	6 780.6						
$V - B$		0.0884 (1)	0.0681 (1)	0.0804 (1)	0.0888 (1)	0.0842 (1)	+0.1046 (1)
$B - U$		0.0339 (1)	0.0205 (1)	0.0464 (1)	0.0209 (1)	0.0418 (1)	-0.0002 (1)
$B - L$		0.0247 (1)	0.0220 (1)	0.0320 (1)	0.0226 (1)	0.0295 (1)	+0.0159 (1)
$U - W$		0.0355 (1)	0.0297 (1)	0.0362 (1)	0.0358 (1)	0.0387 (1)	+0.0464 (1)
$V_j$ from:							
Geneva	8 634-9 044	8.557 (12)				9.747 (5)	7.284 (9)
Strömgren	9 360.5-71.8	8.534 (105)	7.936 (117)	9.381 (64)	8.195 (74)		
Walraven	6 780.6	8.552 (1)	7.951 (1)	9.415 (1)	8.192 (1)	9.742 (1)	7.285 (1)

In the present case, we opted to start the iterative procedure with FOTEL. Although KOREL easily detects partial eclipses without a priori knowledge, the sensitivity of the composite spectrum to light changes is too small to derive useful information from spectra taken with  $S/N = 200$  in the continuum, in comparison to the information available from high precision photoelectric photometry. Moreover, multiple Gaussian fitting on some selected helium lines provides sufficiently precise radial velocities in several orbital phases (Sect. 6.2.1) to obtain, in combination with the *wby* light-curves, good light ratios for subsequent input to KOREL.

KOREL was then applied to spectral regions (Sect. 6.1) selected because of apparent absence of contamination by a third contributor (i.e. the interstellar medium, especially attenuation by diffuse interstellar bands (DIBs)) and because of superior

$S/N$ . Weak contamination (Table 6) was removed interactively. The light ratios were fixed at the values obtained by FOTEL.

FOTEL was then applied once more, with the newly obtained radial velocities for each spectral region as properly weighted data subsets and with unchanged photometric information. Compared to the first application of FOTEL, the weight of the (more precise) velocity data had increased relative to the weight of the photometry.

Further iterations KOREL  $\leftrightarrow$  FOTEL improved the orbital solution, but contributed almost no significant changes in the component spectra. None but the strongest lines in the intrinsic spectra are weakly sensitive to the convergence of the light ratio. At the end of the iteration cycle all selected spectral regions were disentangled with identical, fixed parameters, in order to obtain the spectral components  $S_p$  and  $S_s$ . ‘Final’ radial velocities for

each component were derived as weighted averages over all the wavelength regions analyzed with KOREL. Adding these radial velocities with the proper weight to the light-curves in  $v$ ,  $b$  and  $y$ , we obtained the final dynamical parameters with the WD code. Cuts were made in one-dimensional subspaces of the parameter space to determine the accuracy of the WD solutions.

In addition, the disentangled spectral contributions  $S_p$  and  $S_s$  were normalized to the intrinsic continuum of the related component, giving the ‘intrinsic component spectra’  $S_p^0$  and  $S_s^0$ . These spectra are analyzed just like individual stars. The orbital solution imposes well-determined dynamical gravities from the component masses and radii, which facilitates the determination of the temperature from the intrinsic component spectra. Rotational velocities ( $i$  is known) were measured, using selected spectral regions in the star # 201 (J11) as a template. The systemic velocity is obtained from selected He, Si and O lines.

### 6.1. Fourier disentangling of the composite spectra

First of all, some choices should be specified which were implied by technical limitations in the version of KOREL which is presently available (Sect. 2.2). In order to exploit the spectral resolution of our data, each of the maximum 5 spectral regions that can be combined should not be longer than 100 Å. With 5 regions, 3 components may be considered, allowing the inclusion of an interstellar component. After initial trials on regions covering the whole spectral range, it was decided to divide the spectrum in two kinds of regions:

- those containing strong and diagnostic spectral lines, with low noise, and weak or no contribution from the interstellar or circumstellar medium; obviously, these are the ones best suited to derive orbital and atmospheric parameters;
- those containing a stronger contribution from the interstellar or circumstellar medium, and the more noisy part towards the violet, which could profit from a more robust disentangling once the orbital parameters were fixed using the other spectral regions.

The regions used to derive the orbital parameters are defined in Table 6. These regions were grouped into two data sets, one covering almost 400 Å continuously, the other covering more than 200 Å at longer wavelengths. Each set was fitted separately by KOREL. The weight associated with each region is taken as proportional to the square of the expected value of the local  $S/N$  of each exposure (Fig. 2).

The first KOREL analysis was run with a continuum flux ratio  $C_p/C_s = 2.2$  for all spectra except for s1a and s1b, for which the light ratio in the corresponding eclipse,  $C_p/C_s = 2.84$ , was adopted. The light variability seen out of eclipse may be safely neglected, since it nowhere changes the absorption in the component spectra by more than 0.1% of the combined continuum level  $C_{\text{total}}$ .

An example of the orbital solutions obtained during the iteration cycle, by varying all orbital parameters except  $P_{\text{orb}}$ , independently for set A and set B, is given in Table 7 as KOREL-A

**Table 6.** Spectral regions for spectral disentangling.

Set	Region	Wavelength	Prominent lines	Notes
A	1	4018.5 – 4046.8	He I	
	2	4046.8 – 4139.0	H $\delta$	
	3	4139.0 – 4248.5	He I, metals	IS
	4	4248.5 – 4309.4	metals	IS
	5	4309.4 – 4403.2	H $\gamma$ , He I	
B	6	4459.1 – 4498.6	He I, Mg II	
	7	4536.7 – 4625.7	Si III, O II	weak DIB
	8	4625.7 – 4721.0	He I & II, metals	

and KOREL-B. Although no formal error estimates are listed by KOREL, the internal consistency gives confidence in the procedure. The combined KOREL solution KOREL-AB was found by interpolating in a fine grid for the minimum of the sum of the weighted squared residuals for sets A and B together. The spectra in each region were then disentangled with the orbital parameters of KOREL-AB kept fixed. A small portion of the disentangled spectra and the predicted composite spectra at the observed orbital phases are shown in Fig. 4.

The gain in accuracy in radial-velocity measurements when using KOREL instead of using simple line-centering methods is substantial. The velocities derived by KOREL from individual regions scatter with a rms of 3 km s<sup>-1</sup> (primary) to 4 km s<sup>-1</sup> (secondary) around the combined KOREL solution. For the He lines fitted initially by two Gaussians, this scatter was 4 km s<sup>-1</sup> (primary) to 8 km s<sup>-1</sup> (secondary) at phases with a velocity difference between both components that exceeded 200 km s<sup>-1</sup>, while several much larger residuals were seen in phases where lines were more closely blended. The accuracy obtained from a weighted average over all wavelength regions considered by KOREL is illustrated in Figs. 5 and 6.

As far as random errors are concerned, a *lower limit* to the uncertainty in the radial velocities obtained from KOREL may be estimated in the same way as did Verschueren & David (1999), taking into account that, in a composite spectrum with two components p and s, the function  $F(\delta_p, \delta_s)$  that must be minimized is

$$\sum_j W(j) [I_{\text{obs}}(j) - (I_p(j + \delta_p) + I_s(j + \delta_s) - 1) + \nu(j)]^2 \quad (8)$$

$I_{\text{obs}}(j)$  is the normalized intensity of the observed, composite spectrum, for pixel  $j$ .  $I_p(j + \delta_p) + I_s(j + \delta_s) - 1$  is the template derived by KOREL from a set of spectra observed at different orbital phases, i.e.  $I_p(j + \delta_p)$  is the template for the primary shifted by  $\delta_p$  and  $I_s(j + \delta_s)$  the template for the secondary shifted by  $\delta_s$ .  $\nu$  is the noise on the observed, composite spectrum. It is assumed that the noise in the templates is negligible and uncorrelated with the noise in the input spectra. This is a good approximation when the templates are derived by KOREL from a sufficiently large set of input spectra.  $W$  is the inverse of the expectation value of the variance due to random noise. The summation extends over the spectral region considered.

When only photon shot noise is considered in this two-component case, a simple expression for the variance  $\text{Var}(\delta_k)$

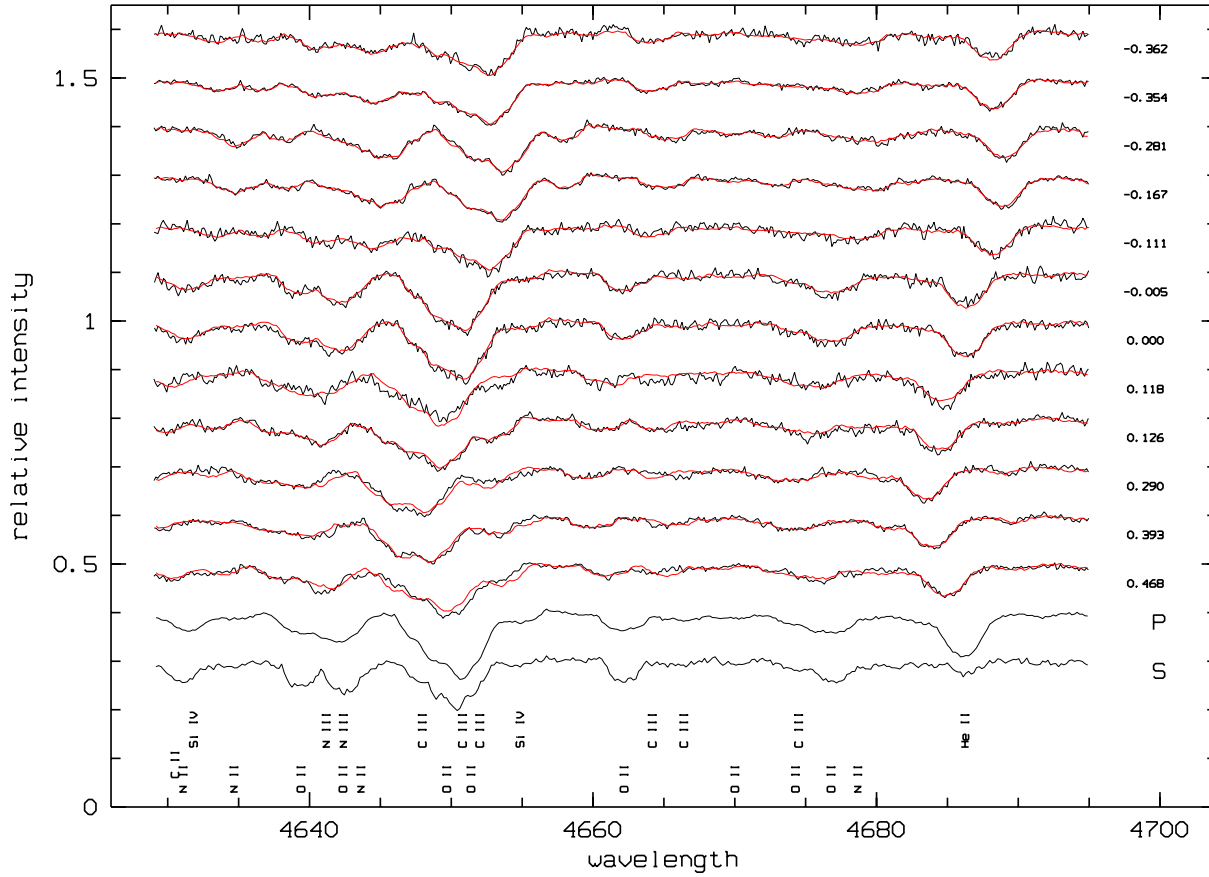


**Fig. 4.** Extract of the observed composite spectra (the orbital phase relative to the primary eclipse is indicated at the r.h.s.) and the disentangled spectra of the hotter (P) and the cooler component (S). The composition of P and S at the observed phases is overplotted, using the appropriate Doppler shifts and relative intensities. Each spectrum is normalized, but shifted over 0.1 with respect to its neighbour.

**Table 7.** Some iterative orbital solutions for V578 Mon during the KOREL-FOTEL iteration cycle. The time of periastron passage,  $T$ , refers to the epoch of the spectroscopy.

Data set	$T$ 2400000+	$e$	$\omega$ [ $^{\circ}$ ]	$K_s$ [ $\text{km s}^{-1}$ ]	$q$
FOTEL-init	$49010.67 \pm 0.01$	$0.088 \pm 0.003$	$151.8 \pm 1.8$	$259.4 \pm 1.6$	$0.709 \pm 0.005$
KOREL-A	49010.685	0.085	154.6	259.3	0.711
KOREL-B	49010.686	0.096	154.5	261.7	0.707
KOREL-AB	49010.685	0.087	154.6	259.7	0.710
FOTEL-fin	$49010.67 \pm 0.01$	$0.0836 \pm 0.0008$	$152.98 \pm 0.8$	$259.8 \pm 0.8$	$0.705 \pm 0.004$

on the shift  $\delta_k$  of the  $k$ -th component can be derived from the explicit minimization of Eq. 8:

$$\text{Var}(\delta_k) = \text{Var}_0(\delta_k) \frac{1}{1-f} \quad (9)$$

The subscript 0 refers to the variance in the case that there would be only one component, i.e. (Verschueren & David 1999):

$$\frac{1}{\text{Var}_0(\delta_k)} = \sum_j W(j) J_{\text{obs}}^2(j) \quad (10)$$

with  $J$  the spectral gradient with respect to the bins  $j$  (logarithmic in wavelength). The generalisation to two components

made in this paper introduces a factor  $f$  that depends on the correlation between the spectral gradients of the components of the combined spectrum, with

$$f = \frac{[\sum_j W(j) J_p(j) J_s(j)]^2}{\sum_j W(j) J_p^2(j) \sum_j W(j) J_s^2(j)} \quad (11)$$

Inclusion of more components and of read-out noise are straightforward, but not important in our case. Note that the uncertainty reduces to the result for a single spectrum when  $\sum_j W(j) J_p(j) J_s(j) = 0$ . The uncertainty on the Doppler shift is significantly larger than for a single spectrum only when the gradients of the shifted component spectra correlate strongly

with each other. This is obviously the case when the spectra of the components are quite similar and only slightly shifted, i.e. deep in eclipse. In our application, the two-component random error estimates (Fig. 6) differ by less than 5% from the single-spectrum estimates except for the spectra s1a and s1b, for which the errors are larger by a factor 1.07–1.60 (s1a) and 1.13–1.94 (s1b) depending on the spectral region. The correlation between spectral gradients is larger in the regions 1, 2 and 5 where one spectral line common to both components dominates.

## 6.2. Light- and radial-velocity variability

### 6.2.1. Details of analysis

The iteration procedure was started by applying FOTEL taking as input the light curves and radial velocities measured by fitting simultaneously two Gaussian profiles to the stronger He I lines  $\lambda\lambda$  4143.759, 4387.928, 4471.507 and 4921.929 Å. As noted in Sect. 6.1, such a fit gave fair velocities when the lines of the components are separated by more than 200 km s<sup>-1</sup>, but there is some zero-point uncertainty in the wavelength of the intrinsically asymmetrical He I features. Since the He II line at 4685.682 Å is vanishingly weak in the secondary, it was included to constrain the velocity of the primary for the spectra taken in eclipse. The preliminary solution FOTEL-init (Table 7) was obtained by weighting the photometric measurements in inverse proportion to the expected values of the variances due to random errors, as listed in Table 5, and scaled such that a measurement with an rms of 2 millimag receives a weight of 2.5. For the velocities, the scaling associates the weight 2.5 to an rms of 0.9 km s<sup>-1</sup>.

In the next iterations, the improved radial velocities for each of the spectral regions defined in Table 6 replaced the Gaussian-fit values. They have now a stronger influence on the solution. The orbital elements changed only marginally, but the formal probable errors computed by FOTEL from the covariance matrix were significantly reduced (see FOTEL-fin in Table 7). Note that the orbital period was kept fixed, because a trial with  $P$  as free parameter returned, within the errors, the value given in Sect. 5, and the latter is based on a much longer baseline.

The final solution for the orbital and physical parameters for the binary system is based on the WD programme. The capabilities of the WD programme are described extensively in the literature by its authors and users; we refer here only to Wilson (1993). First, preliminary light curves were calculated and adjusted to the observed light curves using the main (LC) code within the WD programme for generating light and radial velocity curves. Then, a simultaneous solution for the light and radial velocity variations was performed through differential corrections (the DC code in the WD programme). The number of free parameters was kept as low as possible, as advised when calculating the differential corrections in the process of parameter optimization. It is well known that some parameters are highly correlated. Consequently, when we ran the DC code, we varied in turn multiple subsets of the parameters, as code was run varying in turn multiple subsets of the parameters, as suggested by

**Table 8.** Simultaneous light and radial velocity DC solution for V578 Mon with the WD programme. See Sect. 6.2.1 for the list of optimized parameters and symbol explanation.  $l = L_p/(L_p + L_s)$  denotes the relative luminosity of the primary component, with subscripts referring to the passband. Probable errors are computed as explained in Sect. 6.2.2, except those followed by a semi-colon. The latter should be considered as rough upper limits to the p.e.

Parameter	Value	Error
<hr/>		
Adjusted		
$e$	0.0867	0.0006:
$\omega$ [°]	153.3	0.6:
$A$ [ $R_\odot$ ]	22.03	0.04
$i$ [°]	72.58	0.3
$q$	0.7078	0.0002
$\Omega_p$	5.02	0.05
$\Omega_s$	4.87	0.06
$r_{p,pole}$	0.234	0.0022
$r_{p,point}$	0.243	0.0022
$r_{p,side}$	0.237	0.0022
$r_{p,back}$	0.241	0.0022
$r_{s,pole}$	0.194	0.003
$r_{s,point}$	0.200	0.003
$r_{s,side}$	0.195	0.003
$r_{s,back}$	0.199	0.003
$l_y$	0.692	0.006:
$l_b$	0.683	0.006:
$l_v$	0.675	0.006:
<hr/>		
Not adjusted		
$g_p$	1.0	
$g_s$	1.0	
$A_p$	1.0	
$A_s$	1.0	
$x_{py}$	0.304	
$x_{pb}$	0.335	
$x_{pv}$	0.367	
$x_{sy}$	0.306	
$x_{sb}$	0.342	
$x_{sv}$	0.363	

Wilson & Biermann (1976). Since the effective temperatures of the components are determined from the disentangled component spectra, the WD programme was used exclusively in ‘mode 0’, in which the luminosities are decoupled from the effective temperatures. The orbital elements that were optimized are: eccentricity  $e$ , longitude of periastron  $\omega$ , semi-major axis  $A$  of the orbit, inclination  $i$  and radial velocity of the centre of mass (systemic velocity)  $V_\gamma$ . The adjusted physical parameters of the components are: radii in terms of potential  $\Omega_p$  and  $\Omega_s$ , respectively, mass ratio  $q$  and luminosity  $L_p$  of the primary. The last parameter is wavelength-dependent and its value is determined in each pass-band separately (the final solution was obtained with the  $y$ ,  $b$  and  $v$  light curves, and the KOREL radial velocities for both components). The limb-darkening coefficients for each component and/or pass-band were fixed at the values calculated by Diaz-Cordoves et al. (1995). Albedos and gravity-

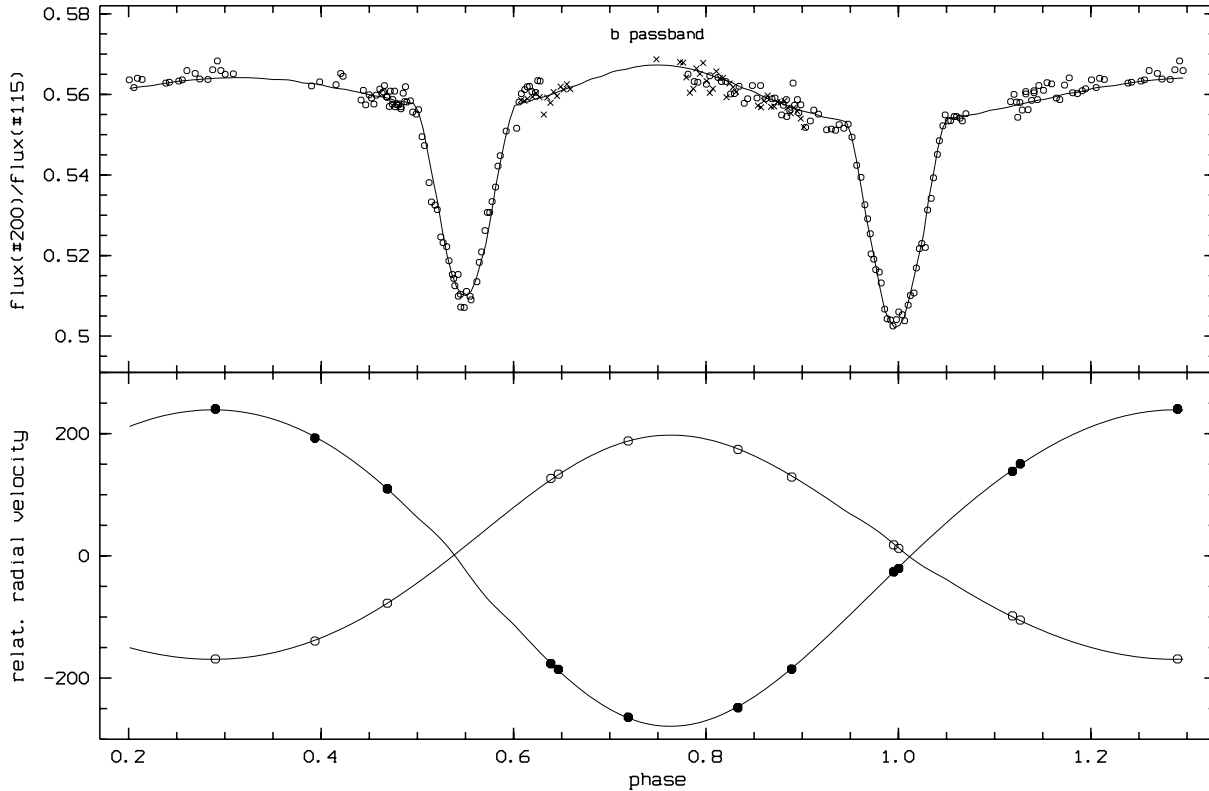


**Fig. 5.** The WD model fitted to the observations. Only one light curve is shown because the colour variations are very small (Fig. 3). Photometric observations by Andersen are indicated by crosses. The radial velocity zero-point is the systemic velocity. Filled symbols refer to the secondary, open circles to the primary component.

darkening coefficients were fixed to the theoretical (canonical) values given in Table 8. The final solution is shown in Fig. 5, while the residuals are displayed in Fig. 6. Orbital parameters are listed in Table 8, and fundamental stellar parameters in Table 9.

### 6.2.2. Accuracy of the orbital solution

Estimating the accuracy of the solution is not simple for a number of reasons. While the method of least-squares minimization implicitly assumes that the deviations of the observations relative to the model are due to random errors, it should be checked whether this assumption holds in practice; the more precise the observations are, the more probable it is that systematic errors, either due to inaccuracies in the models or to systematics in the data, contribute significantly. Furthermore, it is well-known that physically interesting parameters may be strongly coupled.

Our approach to estimate uncertainties in the parameters, that will later be used to estimate the age and distance of V578 Mon's parent stellar cluster, is based on an analysis of the sum of the weighted squared residuals  $\sum_j \Delta(j)$  which directs the convergence process towards the final orbital solution. The summation  $j$  extends over the different light curves and the two radial-velocity curves. The sum may be split into contributions due to random noise,  $\sum_j \Delta_0(j)$ , and contributions due to systematic errors,  $\sum_j \Delta_{sy}(j)$ . In the absence of the latter, WD

models could be readily rejected by comparison of the measured  $\sum_j \Delta(j)$  with the expected value of  $\sum_j \Delta_0(j)$  computed from the expected values of the random errors in the photoelectric photometry (Table 5) and in the radial velocities (Eqs. 9-11), and taking into account the number of data points ( $3 \times 248 + 2 \times 12$ ), and fit parameters (9). Under those conditions, a model could be rejected at the 95% confidence level when the corresponding  $\sum_j \Delta(j)$  exceeded expected value of  $\sum_j \Delta_0(j)$  by a factor 1.087 (see tables of the  $\chi^2$  distribution, e.g. Abramowitz & Stegun 1968).

In our case, systematic errors are significant, although small in an absolute sense. The expected value for  $\sum_j \Delta_0(j)$  turns out to be 0.00758, while the final model has  $\sum_j \Delta(j; \text{final}) = 0.02647$ . Hence, it appears that random noise contributes maybe only 30% to  $\sum_j \Delta(j; \text{final})$  and systematic errors up to 70%. In the case of the photometry, the residuals displayed in Fig. 6 and our success in quantifying random errors in other high-precision photometric programmes that used the same observation and data-reduction technique make it implausible that the random errors could be grossly underestimated. In the case of the radial velocities, we actually computed a lower limit to the random errors (Sect. 6.1) and might have overestimated the contribution of systematic errors. Fig. 6 shows that the velocities measured from the three couples of repeated spectra are consistent with the estimated random errors in the case of the primary, but less so in the case of the secondary.

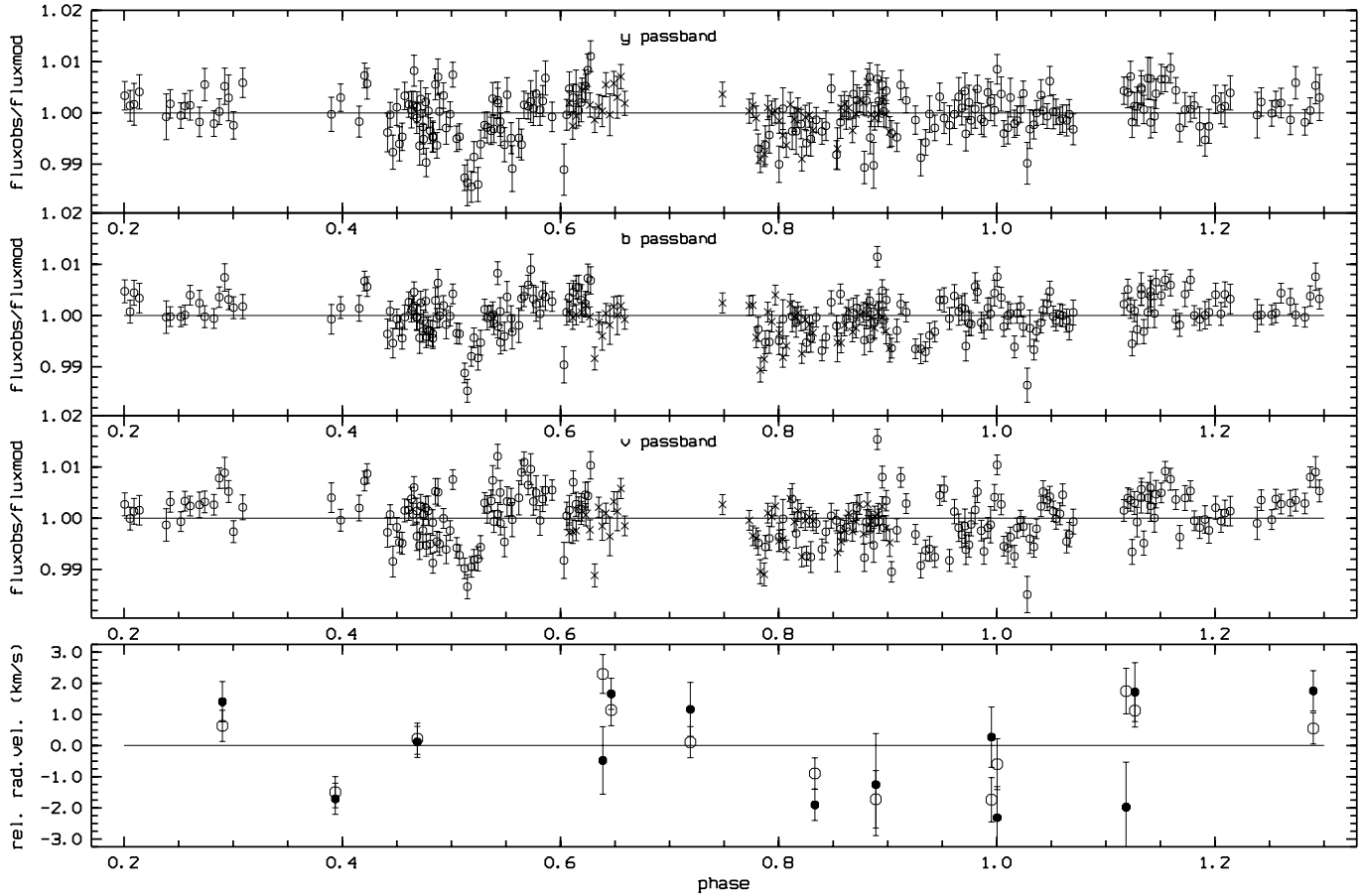


**Fig. 6.** Residuals to the WD model for all photometric passbands used in the final fit and for the radial velocities. Error bars are  $\pm 1\sigma$  estimates of random noise. Photometric observations by Andersen are indicated by crosses. In the radial velocity panel, filled symbols refer to the secondary, open circles to the primary component.

Considering the *absolute* level of the rms scatter due to systematic errors, of the order of 3 millimag and  $1.2 \text{ km s}^{-1}$  (see also Fig. 6), and the physics on which the model is built, such discrepancies are not unexpected. It is possible that apsidal motion within the one-year time interval between spectroscopy and photometry would contribute to such small systematic residuals. An optimistic evaluation of the uncertainties in the WD parameters might be made by assuming that the contribution to the residuals from systematic errors remains unchanged in the vicinity of the best solution, and by neglecting the (unknown) bias introduced by those systematic errors. Under these conditions, WD models have to be rejected at the 95% confidence level using the criterion:

$$\sum_j \Delta(j; \alpha_k, k = 1, \dots, K) > S_{0.95} \equiv 1.087 \sum_j \Delta_0(j) + \sum_j \Delta_{\text{sy}}(j; \text{final}) \quad (12)$$

More explicitly, a parameter value  $\alpha_{k0}$  cannot be rejected at the 95% confidence level when a model with fixed  $\alpha_k = \alpha_{k0}$  can be found (varying all other parameters) that has  $\sum_j \Delta(j; \alpha_1, \dots, \alpha_{k0}, \dots, \alpha_K) < S_{0.95}$ .

In view of our needs and in order to keep the computational overhead limited, the error estimates were derived in detail for some parameters ( $i$ ,  $A$ ,  $\Omega_p$ ,  $\Omega_s$ ) and more approximately for others. In the detailed study, the parameter in question was fixed at a value different from the optimal one and all other parameters were optimized by the WD code. This was repeated for a number of equally spaced values of the fixed parameter, leading to a detailed scan of  $\sum_j \Delta(j)$  for the particular parameter. The 95% confidence interval for this parameter was then defined as the interval over which the scanned  $\sum_j \Delta(j)$  remained below  $S_{0.95}$ . For the remaining parameters listed in Table 8, their variation over all scans falling inside the confidence intervals for the parameters checked in detail was noted; that gives a lower limit to their own confidence intervals. The same rough estimate was made also for the combinations of parameters which are of interest for a specific application, such as  $q$  or the ratio of the radii which enters into the computation of the error in  $\log(\frac{p}{g_s})$ .

The results are listed in Table 8. The uncertainties are scaled to probable errors (dividing the length of the 95% confidence interval, which is very near to  $2\sigma$ , by 2.9). Despite the fact that these p.e. should be considered as lower limits, they are at least a factor 5 larger than the formal errors computed by the WD code.

**Table 9.** Fundamental data for the components of V578 Mon.  $v_{\text{synchr}}$  is the predicted rotational velocity corresponding to synchronisation of the orbital and the rotational period.  $v_{\text{rot}}$  are the rotational velocities derived from the line widths and the orbit inclination. The listed uncertainties are probable errors.

	Primary		Secondary	
Mass [ $M_{\odot}$ ]	14.54	$\pm 0.08$	10.29	$\pm 0.06$
Radius [ $R_{\odot}$ ]	5.23	$\pm 0.06$	4.32	$\pm 0.07$
$\log g$ [cgs]	4.163	$\pm 0.010$	4.179	$\pm 0.013$
$T_{\text{eff}}$ [K]	30 000.	$\pm 500.$	26 400.	$\pm 400.$
$M_{\text{bol}}$ [mag]	-6.00	$\pm 0.05$	-5.03	$\pm 0.075$
$m_V$ [mag]	8.934	$\pm 0.013$	9.813	$\pm 0.020$
$v_{\text{synchr}}$ [ $\text{km s}^{-1}$ ]	110.	$\pm 1.3$	91.	$\pm 1.5$
$v_{\text{rot}}$ [ $\text{km s}^{-1}$ ]	122.	$\pm 3.$	98.	$\pm 2.$

### 6.3. Spectroscopic analysis of individual components

The spectral disentangling yields the component spectra normalized to the sum of the continua of both components ( $C_{\text{total}}$ ). (In fact, each of the components contributing to the observed, composite spectrum is normalized such that its average value over the considered region equals 1). Using the wavelength-dependent light ratio between both components, we may renormalize each of the component spectra to its intrinsic continuum  $C_{\text{comp}}$ . At this stage, all random and systematic errors in the difference between line and continuum flux will be amplified by a factor  $C_{\text{total}}/C_{\text{comp}}$ , i.e. in our case about 1.45 for the brighter component and about 3.2 for the fainter. While this is unavoidable as far as random noise is concerned, this is the moment at which systematic errors arising from different causes (e.g. normalisation of the original spectra, incorrect disentangling possibly due to a neglected component in the spectrum) may become obvious. Such indications are indeed found, especially in the presence of broad DIBs. Experiments have shown that a detailed analysis and removal of the cause, followed by another KOREL iteration might be useful when analyzing metal lines of a few percent depth (note that many lines are not deeper at the rotational velocities involved), in particular where very wide DIBs interfere. For our present purpose – the determination of temperature, gravity and rotational velocity – sufficient clean spectral regions were available and no effort was made to improve and include more complicated spectral regions such as the  $H_{\beta}$  + DIB (4880 Å) structure and the regions around 4520 Å and 4740 Å where there are suspected circumstellar contributions. An abundance analysis and the publication of the detailed component spectra inclusive of the interstellar absorption and possible faint circumstellar signatures is deferred until later.

#### 6.3.1. Projected rotational velocity

The rotational velocity was determined from spectral features fulfilling three necessary conditions:

- other broadening mechanisms should not be too important;
- line blending should be unimportant;
- continuum placement errors should be unimportant.

Random noise is never the limiting factor in our specific case. The first two criteria were evaluated from theoretical spectra, and on an observed spectrum of the sharp-lined early-B star # 201 in NGC 2244 (Vrancken et al. 1997). It was found empirically that local continuum placement errors cancel better when working differentially with respect to the spectrum of # 201, which has been observed with the same instrumentation. Consequently, the widths of the clean spectral features due to C II  $\lambda 4267$ , Si III  $\lambda 4553$ , Si III  $\lambda 4568$ , O II  $\lambda 4591-96$  and O II  $\lambda 4662$  were compared to the widths they have in a set of rotationally broadened templates of the star # 201, rather than to their values in synthetic spectra. The templates were obtained by convolving the observed spectrum with a rotational broadening function (Gray 1976). This leads to  $v_p \sin i = 117 \text{ km s}^{-1}$  and  $v_s \sin i = 94 \text{ km s}^{-1}$ , with a rms scatter of 4 and 2  $\text{km s}^{-1}$  respectively between the results for different lines. The FWHMs of the rotationally broadened, clean spectral lines - which are intrinsically sharp - are not sensitive to the difference in atmospheric parameters between the template and the components of V578 Mon. However, even for the stronger metal lines we selected, a change of 0.5% in the continuum placement could influence the measured velocity by as much as 10  $\text{km s}^{-1}$ . From the achieved consistency from different lines and from our judgment of continuum uncertainties, we estimate that systematic errors in the projected rotational velocities does not exceed 3  $\text{km s}^{-1}$ .

Synchronous rotation requires  $v_p \sin i = 104.8 \pm 1.2 \text{ km s}^{-1}$  and  $v_s \sin i = 86.6 \pm 1.4 \text{ km s}^{-1}$ , where the quoted uncertainties are probable errors (p.e.). There are observational evidences (see Claret et al. (1995) and references therein) that eccentric systems are pseudo-synchronized, i.e. their rotational velocities are equal to the orbital velocities at periastron. This condition requires in our case projected rotational velocities of  $125.2 \pm 1.5 \text{ km s}^{-1}$  and  $103.4 \pm 1.7 \text{ km s}^{-1}$ . The observed projected rotational velocities lie in between these estimates and confirm that the system is at least very near to synchronisation.

#### 6.3.2. Atmospheric parameters

In order to constrain the effective temperature and gravity, lines of H, He I, He II, Si III and Si IV were compared to a grid of theoretical spectra (Sect. 2.2) which were rotationally broadened to the projected rotational velocities derived in Sect. 6.3.1. The constraints are graphically summarized in Fig. 7. Different types of lines were analyzed in different ways. For the hydrogen lines a least-squares fit was made to the observed profiles (after the metal lines were removed) keeping the temperature, gravity and continuum level as free parameters. Following Vrancken et al. (1997), we used the part of the hydrogen line with residual intensities between 70% and 99%; we found that the continuum should be put slightly above the originally estimated pseudo-continuum.

The equivalent widths,  $W$ , of the Si lines were measured over the full rotational width. Allowance was made for blending lines before comparing the measurement with theoretical equivalent widths,  $W(\text{th})$  (see note to Table 10), by adding to  $W(\text{th})$  the contribution of the blending lines over the cor-

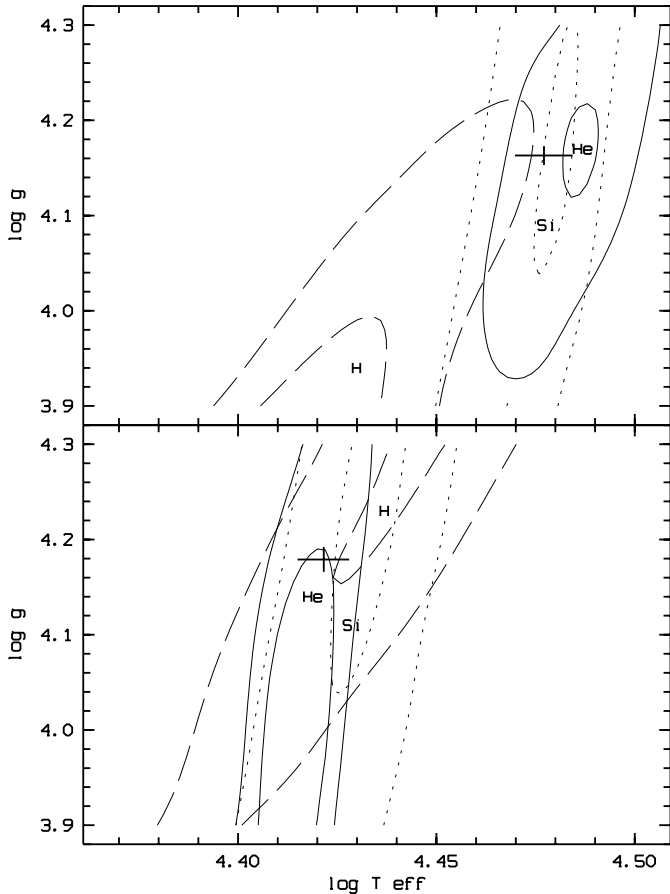


**Fig. 7.** Constraints for  $T_{\text{eff}}$  and  $\log g$  from lines of H (long-dashed), He (full line) and Si (dotted). Two levels of goodness-of-fit are shown for each ion, to indicate which parameter combinations give acceptable fits and – by tightening the requirements – to indicate where the best solutions for a given ion are found. The upper panel refers to the primary, the lower panel to the secondary. Note that the gravity for the final model (indicated in each panel by a cross whose size is defined by the probable errors) was taken from the dynamical analysis rather than the spectroscopic one.

responding wavelength interval of the rotationally broadened synthetic spectra. Solar abundances were assumed. This is a useful approximation in the case of minor blends. Then, the quantity

$$\sum_{\text{lines}} \left( \frac{W - W(\text{th})}{\sigma_W} \right)^2 \quad (13)$$

is used as a measure of goodness-of-fit for the data. Measured and predicted equivalent widths for the final model are collected in Table 10.

The He II lines have broad shallow wings which are not easily measurable in real spectra. Since the accuracy of the measurement is always important to define constraints, the line absorption was measured over the part of the line where it was accurately measurable and compared to exactly the same quantity as derived from theoretical profiles, suitably broadened by rotation. The theoretical profiles were used to give an indica-

tion of which fraction of the total equivalent width should be contained in the chosen interval (Table 11). Finally, the He I lines at 4026 Å, 4388 Å and 4471 Å were compared to theoretical profiles. As is well known, these lines do not constrain the temperature strongly in early-B stars, but their dependence on gravity complements the temperature constraints given by the He II lines.

Taking all the evidence together, we conclude that acceptable fits for all lines are obtained within  $T_{\text{eff}} = 30\,000 \text{ K} \pm 500 \text{ K}$  and  $\log g = 4.2 \pm 0.1$  for the primary component and within  $T_{\text{eff}} = 26\,400 \pm 400 \text{ K}$  and  $\log g = 4.15 \pm 0.15$  for the secondary. Note that the spectroscopic gravities agree, within their error bars, with the dynamically derived gravities.

For the primary, the largest discrepancy with the models lies in the H lines. The mathematically best fits are obtained for a low temperature and gravity, but those are excluded by the He and Si lines. Increasing both temperature and gravity and slightly modifying the continuum level allows the predicted profiles to approximate well to the observed width and depth (Fig. 8). At the dynamically derived gravity, the best fit for the H lines still indicates a temperature that is 700 K lower than that derived from the He and Si lines. Our temperature estimate is a compromise. The fact that the red wing of He I  $\lambda 4026$  (Fig. 9) is not properly reproduced is probably caused by the model, as the same problem is observed for the cooler component (and for the star #201, Vrancken et al. 1997). It is interesting to note that the asymmetry seen in the multi-component feature He I  $\lambda 4471$  in the hotter star is slightly different from that seen in the cooler component. Theoretically it can be shown to arise primarily from the small difference in rotational velocity between the two components. This emphasizes that care should be exercised when using such lines for precise velocity determinations. The strength of the He II lines is well reproduced, given that an uncertainty of only 0.25% in the continuum level would change the partial equivalent widths  $w$  by 18 mÅ for the two weaker lines and by 11 mÅ for the  $\lambda 4686$  line.

In the case of the cooler secondary, the H lines fit very well, even quite deep in the core, in contrast to the result for #201 (Vrancken et al. 1997). A differential line-by-line comparison with the rotationally-broadened spectrum of #201 supports the slightly lower temperature and lower gravity of the secondary component of #200 (relative to #201). The He I lines in the secondary are narrower and systematically 3–4% less deep, consistent with the difference in gravity (#201 has  $\log g = 4.3 \pm 0.1$ ). The slightly weaker He II  $\lambda 4686$  line conforms to the lower temperature (#201 has  $T_{\text{eff}} = 27\,300 \text{ K}$ ). The strength of the Si III lines is at most 10% higher than in #201, while that of the Si IV lines is at most 25% lower, but the hypothesis that they have the same strength in both stars cannot be rejected with high significance.

### 6.3.3. Systemic velocity

The systemic velocity  $V_\gamma$  was derived from individual line positions in the disentangled spectra, by comparison with their laboratory wavelengths (Table 12). The lines were selected on

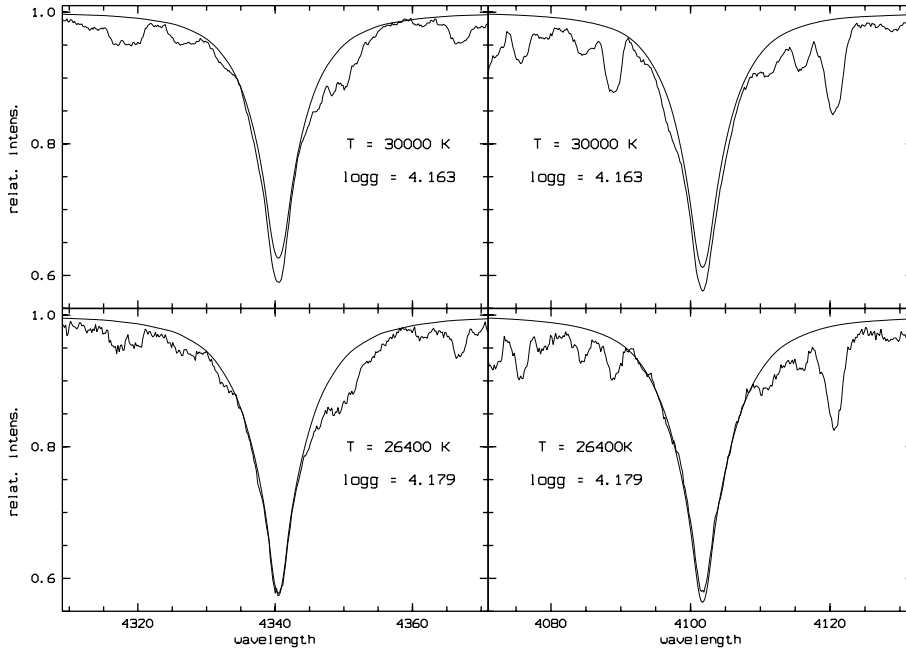


**Fig. 8.** The Balmer lines  $H\gamma$  and  $H\delta$  for the primary (upper panels) and the secondary component of V578 Mon, after disentangling the composite spectrum and normalising to the component's continua. The model shown for comparison corresponds to the finally accepted  $T_{\text{eff}}$  and  $\log g$ , rather than to the mathematically best fit for hydrogen alone. The theoretical profiles are shifted according to  $V_{\gamma} = 34.9 \text{ km s}^{-1}$ .

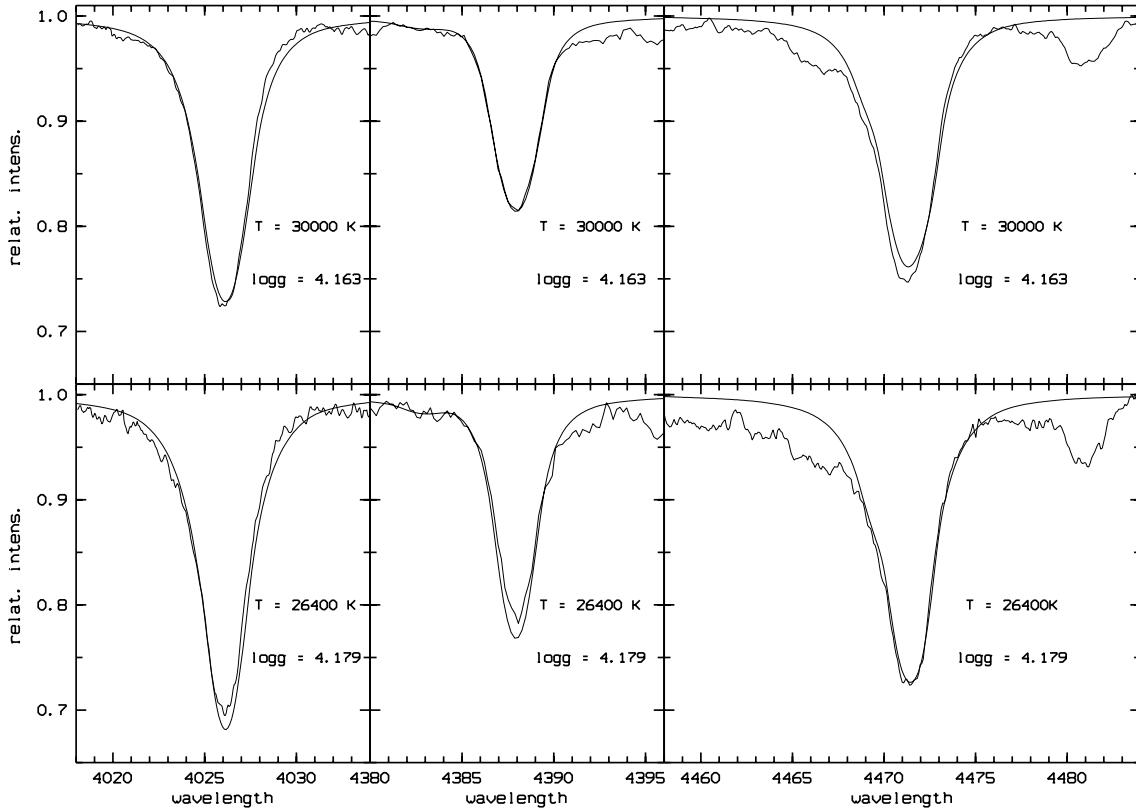


**Fig. 9.** The He I lines  $\lambda\lambda$  4026, 4388 and 4471 Å for the primary (upper panels) and the secondary component of V578 Mon, presented in a similar way as the Balmer lines in Fig. 8.

the basis of their strengths and symmetry. The symmetry was empirically checked by measuring the line position within a set of wavelength intervals, gradually expanding from just the deep core out to the full width at the continuum. Acceptable lines gave consistent position estimates (no significant trend with interval

length) at least up to a width of 3 Å, i.e. including more than 80% of the full rotational width. The most obvious asymmetry which is probably not due to blending is seen in the He II  $\lambda$ 4486 line, with velocity estimates varying smoothly from 28 km s<sup>-1</sup> for the core of the line (2-Å interval), down to 25 km s<sup>-1</sup> when

**Table 10.** Measured equivalent widths for selected Si lines. The theoretical equivalent widths refer to the final model parameters (Table 9), a solar Si abundance and a microturbulent velocity  $v_t = 1 \text{ km s}^{-1}$ . The numbers between brackets indicate the uncertainties in  $W_p(\text{th})$  and  $W_s(\text{th})$  according to the temperature ranges  $T_{\text{eff}}(\text{p}) = (29\,500, 30\,500) \text{ K}$  and  $T_{\text{eff}}(\text{s}) = (26\,000, 26\,800) \text{ K}$ , respectively.

ion	wavelength [Å]	$W_p$ [mÅ]	$W_p(\text{th})$ [mÅ]		$W_s$ [mÅ]	$W_s(\text{th})$ [mÅ]	
Si IV	4116.1	120*	112	(104,117)	50*	57	(51,64)
Si IV	4212.4	36	44	(40,47)	17	14	(12,17)
Si III	4552.6	<146**	134	(142,124)	<210**	169	(170,168)
Si III	4567.8	114	114	(121,105)	145	146	(146,145)
Si III	4574.8	71	73	(78,65)	95	98	(99,98)
Si IV	4654.3	<100***	78	(70,82)	35:***	25	(20,30)

\* Si III 4115.487 contributes weakly

\*\* includes N II  $\lambda 4552.522$ ; estimated 130: mÅ(p), 160: mÅ(s) without this blending line

\*\*\* wing of  $\lambda 4650$  blend complicates measurement

**Table 11.** Measurements of He II lines and values for the final model parameters (Table 9).  $W$  indicates the total equivalent width,  $w$  the one that refers to the measurement interval  $iw_p$  or  $iw_s$ . A solar He abundance is assumed. Only one line is detected in the cooler component, in agreement with the theoretical prediction.

ion	wavelength [Å]	$iw_p$ [Å]	$w_p$ [mÅ]	$w_p(\text{th})$ [mÅ]	$W_p(\text{th})$ [mÅ]	$iw_s$ [Å]	$w_s$ [mÅ]	$w_s(\text{th})$ [mÅ]	$W_s(\text{th})$ [mÅ]
He II	4199.8	4196.89-4203.99	60:*	74	122				
He II	4541.6	4537.54-4544.64	92	103	141				
He II	4685.7	4683.83-4688.33	261	219	269	4684.33-4686.83	47	49	63

\* measured as 103 mÅ; the contribution of N III  $\lambda 4200.074$  and N II  $\lambda 4199.977$  in the measurement interval is estimated to be 43 mÅ.

**Table 12.** Velocity shifts for selected lines in the disentangled spectra of the primary and the secondary component. Error estimates include effects of noise, consistency of measurement over intervals of different widths, and the effect of a slight error of  $2 \cdot 10^{-4} \text{ \AA}^{-1}$  in the continuum slope.

$\lambda_{\text{lab}}$ Å	ident.	$\Delta \lambda_p$ Å	$\Delta \lambda_s$ Å	$\Delta v_p \pm \sigma$ $\text{km s}^{-1}$	$\Delta v_s \pm \sigma$ $\text{km s}^{-1}$
4143.795	He I	0.546	0.553	$39.6 \pm 0.8$	$40.0 \pm 1.7$
4387.928	He I	0.516	0.570	$35.3 \pm 0.7$	$39.0 \pm 3.3$
4552.654	Si III	0.441	0.492	$29.1 \pm 1.5$	$32.4 \pm 2.0$
4567.872	Si III	0.576	0.542	$37.8 \pm 2.0$	$35.6 \pm 3.2$
4590.971	O II	asym*	0.461		$30.1 \pm 2.4$
4596.174	O II	0.531	0.493	$34.6 \pm 2.0$	$32.2 \pm 1.8$
4661.635	O II	0.523	0.538	$33.7 \pm 2.3$	$34.6 \pm 2.4$

\* apparently blended with a line at a slightly longer wavelength

measured over a 4-Å interval that still does not include the broad wings of the line, and down further to  $19 \text{ km s}^{-1}$  when those wings are included.

The data in Table 12 show that for each line the results are consistent for both components, but indicate that the He I lines might give a slightly different result from the Si III and O II lines. This warns against giving them too much weight, and hence a straight average over all lines is preferred as the best estimate of the systemic velocity:  $V_\gamma = 34.9 \pm 1.0 \text{ km s}^{-1}$ . Cross-correlation between each of the binary component spectra and the correspondingly broadened templates derived from star # 201, over

these small, selected wavelength intervals, leads to a small relative velocity  $\Delta V_\gamma (\#200 - \#201) = -0.8 \pm 1.2 \text{ km s}^{-1}$ , as would be expected between two members of a cluster.

## 7. NGC 2244

### 7.1. Distance

From the radii and effective temperatures for each component of the binary system, the absolute bolometric magnitudes  $M_{\text{bol}}$  may be derived. The apparent brightness  $m_V$  of each component is determined by the observed visual brightness of the binary and the light ratio calculated from the photometric analysis. The distance to the binary can thus be estimated, and therefore the distance to the cluster NGC 2244 of which it is a member, and to the Rosette nebula in which the cluster is embedded.

The absolute magnitude  $M_V$  is related to distance by definition:

$$M_V = M_{\text{bol}} - BC = m_V + 5 - 5 \log d - A_V, \quad (14)$$

where  $d$  is the distance in pc,  $A_V$  is the interstellar absorption in magnitudes, and  $BC$  is the bolometric correction in magnitudes. In a more suitable form:

$$\log d = 0.2(m_V - A_V + BC) + \log R + 2 \log T_{\text{eff}} + K \quad (15)$$

where the constant  $K$  is defined by the fundamental solar data:

$$K = 1 - 0.2(M_{\text{bol}\odot} + 10 \log T_{\text{eff}\odot}) \quad (16)$$

Bessell et al. (1998) recently reviewed critically the zeropoint of the bolometric magnitude scale and the solar constants involved.

From their Appendix D, we selected  $M_{\text{bol}\odot} = 4.74$  mag and  $T_{\text{eff}\odot} = 5781$  K, which yield  $K = -7.472$ . We used the empirical calibration of  $BC$  versus  $T_{\text{eff}}$  by Malagnini et al. (1986), which incorporates the energy distributions for O9-G5 stars observed by them and the data of Code et al. (1976) for stars for which the apparent angular diameters were known from interferometric measurements, and determined  $BC_{\text{p}} = -2.91 \pm 0.13$  mag and  $BC_{\text{s}} = -2.60 \pm 0.09$  mag. The associated probable errors are estimated from the uncertainties given in the papers cited above. The interstellar extinction  $A_V = 1.41 \pm 0.09$  mag was derived from Walraven  $VBLUW$  photometry of stars in NGC 2244 (Verschueren 1991). The p.e. includes the random errors in  $E_{V-B}$ , an uncertainty of 0.07 in the value of  $R = 3.2$ , the ratio of total to selective absorption (based on the scatter in  $R$  found for individual stars by Pérez et al. (1987)) and an uncertainty of 0.005 in  $E_{V-B}$  due to slightly inhomogeneous reddening in this part of the central hole in the Rosette nebula.

Considering the error budget in the distance calculation, it should be noticed that the dependence of  $BC$  on temperature actually reduces the error on  $2 \log T_{\text{eff}} + 0.2BC$  to the level of the error on  $\log T_{\text{eff}}$ . In order of importance, the contributions to the error in  $\log d$  arise from (i) the intrinsic uncertainty in  $BC$  (contributing to the p.e. 0.026 and 0.018 for primary and secondary, respectively), (ii) the uncertainty in the interstellar extinction (0.018), (iii) the uncertainty in  $2 \log T_{\text{eff}} + 0.2BC$  (0.007 and 0.009 respectively) and radius (0.005 and 0.007 respectively), and (iv) the uncertainty in the apparent visual magnitude (contributing 0.002 to the p.e.). Clearly, the fundamental stellar parameters are determined with sufficient accuracy in the sense that their uncertainties play a minor role in the error budget in the distance. The determination of temperatures from disentangled spectra plays an essential role here. In order to improve the accuracy of the distance, the bolometric flux should be measured more precisely. Assuming that all the listed error sources contribute as independent variances, the relative error in the distance is estimated to be 8% when derived from the data for the primary component and 7% when the secondary is used.

Inserting into Eq. 14 the data of Table 9 and the interstellar extinction and  $BC$  mentioned in this subsection, we find

$$d_{\text{p}} = 1.33 \text{ kpc} \quad \text{and} \quad d_{\text{s}} = 1.47 \text{ kpc}. \quad (17)$$

When the results for the two components are expressed as a ratio, the uncertainty in  $\log(d_{\text{p}}/d_{\text{s}})$  is reduced. Only the errors induced by the uncertainty in the temperatures are independent, but the ratio of the radii is known more precisely (p.e. 0.85%) than the radii themselves. Errors in interstellar extinction cancel and offset errors in  $BC$  are not independent for the small temperature difference between the stars (adopted p.e. of 0.04 in  $\Delta BC$ ). With the quoted error estimates, the probable error in  $d_{\text{p}} - d_{\text{s}}$  is 40 pc. Hence, the difference between the distance estimates obtained from the primary and the secondary component is marginally significant (3.5 p.e.), indicating that the uncertainty in some of the parameters might have been underestimated. In Sect. 7.2 it is shown that the fundamental parameters for the primary are internally consistent with theoretical models for single stars, while there is a marginal inconsistency for

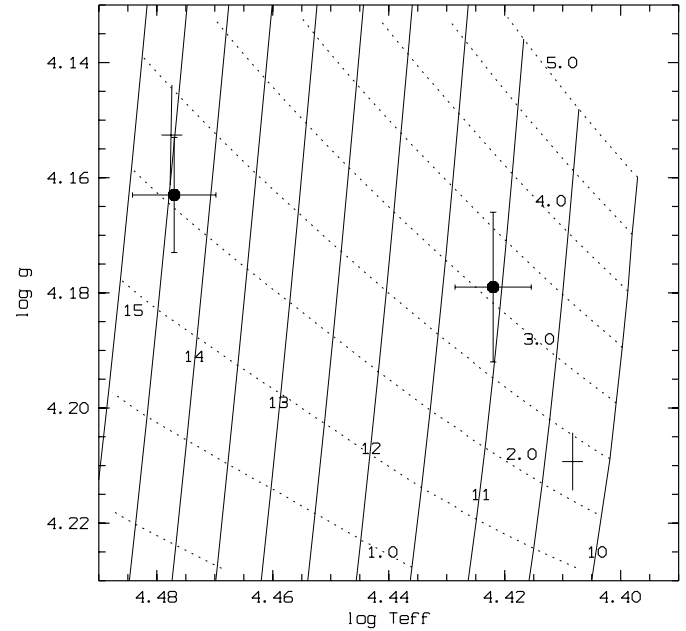


**Fig. 10.** The components of V578 Mon in the  $(T_{\text{eff}}, \log g)$  plane, in a grid of isochrones and evolution tracks interpolated from Schaller et al. (1992). The tracks enclose the mass interval from 10 to  $15 M_{\odot}$ , the isochrones the age interval from 0.5 to  $5 \cdot 10^6$  yr, as indicated by the labels. Filled circles with error bars (p.e.) indicate the position derived from the observations. The crosses indicate the theoretical single star positions corresponding to the dynamically derived masses and their common age (Eq. 19); their size is determined by the p.e. on age and masses only.

the secondary when the error estimates are taken at face value. Therefore, we base our final distance estimate on a weighted average of  $d_{\text{p}}$  and  $d_{\text{s}}$ , having weights  $w_{\text{p}} = 0.6$  and  $w_{\text{s}} = 0.4$  estimated from the variances contributing to the uncertainties in  $d_{\text{p}} - d_{\text{s}}$ :

$$d_{\text{NGC 2244}} = 1.39 \pm 0.1 \text{ kpc}, \quad (18)$$

where the error estimate of 7% reflects mainly the possible offsets in  $BC$  and interstellar extinction. We will speculate about the possible reasons for the marginal inconsistency between  $d_{\text{p}}$  and  $d_{\text{s}}$  in Sect. 8.

## 7.2. Age

The age of V578 Mon was estimated by reference to the evolutionary models of Schaller et al. (1992). Figs. 10 and 11 show the positions of both components relative to a grid of evolutionary tracks and isochrones in the planes of temperature vs. gravity and temperature vs. luminosity. Assuming that the observed masses are correct, requiring that both stars should be on the same isochrone, and taking into account the errors in the empirical quantities, we determined the mathematically best solution for the age and its probable error from a  $\chi^2$  analysis:

$$\text{Age (V578 Mon)} = (2.3 \pm 0.2) \cdot 10^6 \text{ yr} \quad (19)$$

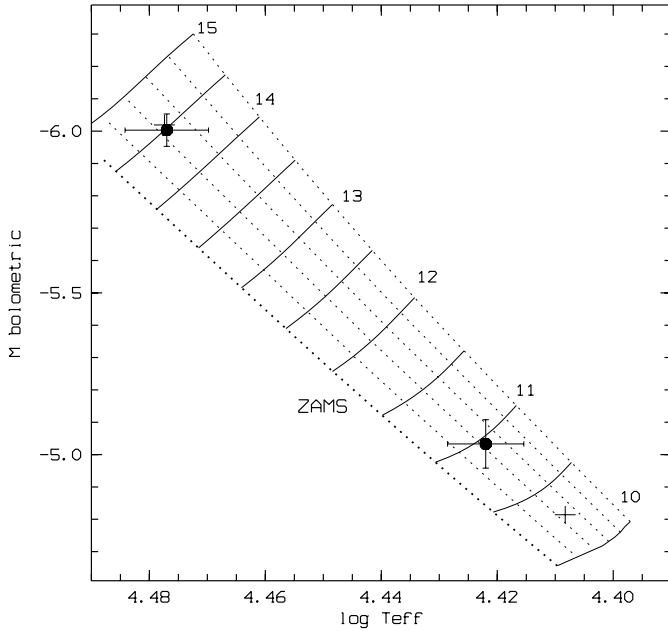


**Fig. 11.** The components of V578 Mon in the  $(T_{\text{eff}}, M_{\text{bol}})$  plane, in a grid of isochrones and evolution tracks interpolated from Schaller et al. (1992). The ZAMS is represented by a thicker dotted line and isochrones correspond to steps of  $10^6$  yr. Symbols are further as in Fig. 10.

Although evolutionary tracks computed by different researchers agree well near the ZAMS, the choice of a particular set may introduce a bias in the age that is of the same size as the formal p.e. derived in this way (e.g. the tracks of Claret (1995) lead to a  $0.4 \cdot 10^6$  yr younger age). The fundamental physical parameters derived for the primary star are internally consistent, while the position of the secondary in the diagrams is only marginally consistent (at the level of 3 p.e.) with the theoretical prediction for a single star of the same mass and age, independent of the particular set of evolutionary tracks. The secondary appears slightly hotter and larger than expected. It remains to be seen whether the spectroscopically derived temperature is overestimated by about 800 K or whether the surface of the secondary is somewhat hotter than it would be for a single star, owing to the proximity of the primary. The discrepancy in the gravity is more probably related to the slight mismatch between the observations and the model in the partial secondary eclipse (Figs. 5 and 6), which possibly biased the value for  $R_s$ . For the present set of observations and the applied dynamical model, a change in the gravity of the secondary would affect directly the estimate of the gravity of the primary ( $\log g_p - \log g_s = 0.016 \pm 0.008$ ), so the empirically derived contrast in gravity also differs at the level of 3 p.e. from that predicted by single star models ( $\Delta \log g \approx 0.04$ ). The age estimate is not very sensitive to these marginal discrepancies. The primary alone appears to have an age of  $2.05 \cdot 10^6$  yr, which only differs by about 1 p.e. from the estimate derived for both components.

## 8. Discussion

V578 Mon is a double-lined eclipsing binary that deserves special attention because of its membership of the young stellar cluster NGC 2244. A set of high-resolution spectra, obtained at 9 phases well spread over the orbit, and *uvby* photometric light curves were used to determine the orbit and to derive the fundamental physical parameters of both components. Some of these stellar parameters were determined directly from the disentangled component spectra. The binary consists of a primary with a mass of  $14.5 M_{\odot}$  and a secondary with a mass of  $10.3 M_{\odot}$ , both well inside their Roche lobe. Nevertheless, small effects of ellipsoidality are seen outside eclipse. The eclipses are partial because of the fairly low inclination,  $72.6^{\circ}$ . The stars move in an eccentric orbit. This is not unexpected since competing theories of the tidal evolution in close binaries (Zahn 1975, Zahn 1992 and references therein; Tassoul 1987, Tassoul & Tassoul 1992 and references therein) both predict a circularisation time scale of  $7 \cdot 10^6$  yr. Since the system is a factor of 3 younger than that, the eccentricity must still be near its initial value. The time-scale for synchronisation depends strongly on which of Zahn's or Tassoul's theories are applied, but is in either case definitely shorter than  $10^5$  yr. The measured rotational velocities are 10% higher at face value than predicted by the dynamical analysis. The most straightforward test for the reality of any deviation from synchronism would be to test the stability of the light curve over a continuous sequence of many rotation cycles.

V578 Mon provides an unique opportunity to estimate the distance to and the age of NGC 2244 using stellar luminosities derived directly from the measured stellar radii and spectroscopic temperatures. Previous distance estimates rely on various calibrations of bolometric magnitude in terms of photometric or spectroscopic luminosity indicators. Once it was settled that  $R = A_V/E_{B-V}$  is not anomalous in the region of the Rosette nebula (Turner 1976; see Pérez et al. (1987) for  $R$  values for individual stars), all 'photometric' distance estimates clustered between 1.42 and 1.70 kpc (Turner 1976, Heiser 1977, Ogura & Ishida 1981, Guseva et al. 1984, Millward & Walker 1985, Pérez et al. 1987, Verschueren 1991). The differences depend mainly on the selection of the cluster members, though also on the calibrations and on  $R$ . Our distance estimate places NGC 2244 somewhat nearer, at  $1.39 \pm 0.1$  kpc. This is what might be expected, given that undetected binarity should have biased the previous estimates towards larger values.

NGC 2244 is known as the youngest subgroup of the Mon OB2 complex. From isochrone fitting, Turner (1976), Heiser (1977) and Ogura & Ishida (1981) derive ages in the range of  $3\text{--}4 \cdot 10^6$  yr. Pérez (1991) applied an alternative, statistical age estimation method, developed by Schroeder & Comins (1988) for the youngest clusters, after Stahler (1985) indicated that isochrone fitting might not give reliable ages in that case. Application to NGC 2244 for stars with masses between  $5.8$  and  $24.4 M_{\odot}$  allowed Pérez (1991) to give limits of  $1.5$  to  $3.6 \cdot 10^6$  yr, with a most probable value of  $2.16 \cdot 10^6$  yr. Our analysis of V578 Mon confirms that NGC 2244 is definitely younger than  $3 \cdot 10^6$  yr. The derived age of  $2.3 \pm 0.2 \cdot 10^6$  yr may

turn out to be still too high if, owing to the proximity of the primary, the secondary component is indeed hotter and somewhat larger than a single star of the same mass. Taking into account the observational and model uncertainties, we can safely conclude that the system is  $1.7\text{--}2.5 \cdot 10^6$  yr old. According to the evolutionary tracks by Palla & Stahler (1993), the ZAMS of NGC 2244 should then extend down to stellar masses of  $3 M_{\odot}$ , corresponding to a spectral type B8-B9V.

*Acknowledgements.* We thank A. Blaauw and M. Sahu for merging observing runs, which allowed us to obtain spectra over the whole orbit. We thank J. Andersen and P. Lampens for their cooperation in the early phases of this project, trying to catch the eclipses, and for making available their photometric data. D. Hall is acknowledged for information on older photometry, partly by amateur astronomers, and on his preliminary analysis of apsidal motion. P. Hadrava is acknowledged for discussions on, and advice with, the KOREL software. E. Griffin is acknowledged for many suggestions, as well on the science as on the grammatical level. The referee, C.A. Prieto, is acknowledged for her constructive comments which contribute to improve the presentation of the paper. This research was carried out in the framework of the project 'IUAP P4/05' financed by DWTC/SSTC. KP acknowledges funding through a fellowship financed by DWTC/SSTC, which made possible a long-term visit to the Royal Observatory of Belgium, Brussels, and through grant #007002 of the Croatian Ministry of Science and Technology. Data reduction and analysis made extensive use of the ESO-MIDAS software, the KOREL, FOTEL and Wilson-Devinney programmes, and the CCP7 library.

## References

- Abramowitz M., Stegun I.A., 1968, *Handbook of Mathematical Functions*. Dover Publ., New York
- Bagnuolo W.G. Jr., Gies D.R., 1991, *ApJ* 376, 266
- Barnard A.J., Cooper J., Shamey L.J., 1969, *A&A* 1, 28
- Barnard A.J., Cooper J., Smith E.W., 1974, *JQSRT* 14, 1025
- Bennett S.M., Griem H.R., 1971, *Techn. Rep. 71-097*, Univ. of Maryland, College Park, Maryland
- Bessell M., Castelli F., Plez B., 1998, *A&A* 333, 231
- Butler K., Giddings J.R., 1985, *CCP7 Newsletter No. 9*, 7
- Claret A., 1995, *A&AS* 109, 441
- Claret A., Giménez A., Cunha N.C.S., 1995, *A&A* 299, 724
- Code A.D., Davis J., Bless R.C., Hanbury Brown R., 1976, *ApJ* 203, 417
- Cox P., Deharveng L., Leene A., 1990, *A&A* 230, 181
- Crawford D., 1975, *PASP* 87, 481
- Diaz-Cordoves J., Claret A., Giménez A., 1995, *A&AS* 110, 329
- Giddings J., 1981, *Ph.D. Thesis*, University of London
- Gray D.F., 1976, *The observation and Analysis of Stellar Photospheres*. John Wiley and Sons, New York, p. 398
- Gray R.O., Olsen E.H., 1991, *A&AS* 87, 541
- Guseva N.G., Kolesnik I.G., Kravchuk S.G., 1984, *SvA Lett.* 10, 309
- Hadrava P., 1990, *Contr. Astron. Obs. Skalnaté Pleso* 20, 23
- Hadrava P., 1995, *A&AS* 114, 393
- Hadrava P., 1997, *A&AS* 122, 581
- Hadrava P., 1998, *KOREL – user's guide* (internal report)
- Hall D.S., 1994, private communication
- Harries T.J., Hilditch R.W., 1998, In: Howarth I. (ed.) *Properties of Hot, Luminous Stars*. ASP Conf. Ser. 131, p. 401
- Hayford P., 1932, *Lick Obs. Bull.* 16, 53
- Heiser A.M., 1971, *BAAS* 3, 66
- Heiser A.M., 1972, *BAAS* 4, 27
- Heiser A.M., 1977, *AJ* 82, 973
- Hiltner W.A., 1956, *ApJS* 2, 389
- Johnson H.L., 1962, *ApJ* 136, 1135
- Kurucz R.L., 1992, *Rev. Mex. Astron. Astrofis.* 23, 45
- Malagnini M.L., Morossi C., Rossi L., Kurucz R.L., 1986, *A&A* 162, 140
- Marschall L.A., van Altena W.F., Chiu L.-T. G., 1982, *AJ* 87, 1497
- Millward C.G., Walker G.A.H., 1985, *ApJS* 57, 63
- Morgan W.W., Hiltner W.A., Neff J.S., et al., 1965, *ApJ* 142, 974
- Ogura K., Ishida K., 1981, *PASJ* 33, 149
- Olsen E.H., 1983, *A&AS* 54, 55
- Olsen E.H., 1993, *A&AS* 102, 89
- Palla F., Stahler S.W., 1993, *ApJ* 418, 414
- Pérez M.R., 1991, *Rev. Mex. Astron. Astrofis.* 22, 99
- Pérez M.R., Thé P.S., Westerlund B.E., 1987, *PASP* 99, 1050
- Sanford R.F., 1949, *ApJ* 110, 117
- Schaller G., Schaerer G., Meynet G., Maeder A., 1992, *A&AS* 96, 269
- Schöning T., Butler K., 1989a, *A&A* 219, 326
- Schöning T., Butler K., 1989b, *A&AS* 78, 51
- Schroeder M.C., Comins N.F., 1988, *ApJ* 326, 756
- Simkin S., 1974, *A&A* 31, 129
- Simon K.P., Sturm E., 1992, In: Grosbol P.J., de Ruijsscher R.C.E. (eds.) *Proc. 4<sup>th</sup> ESO/ST-ECF Data Analysis Workshop*, ESO, p. 91
- Simon K.P., Sturm E., 1994, *A&A* 281, 286
- Stahler S.W., 1985, *ApJ* 293, 207
- Tassoul J.L., 1987, *ApJ* 322, 856
- Tassoul J.L., Tassoul M., 1992, *ApJ* 395, 259
- Turner D.G., 1976, *ApJ* 210, 65
- Verschueren W., 1991, *Ph.D. Thesis*, Free Univ. of Brussels (VUB), Belgium
- Verschueren W., David M., 1999, *A&AS* 136, 591
- Verschueren W., Brown A.G.A., Hensberge H., et al., 1997, *PASP* 109, 868
- Vidal C.R., Cooper J., Smith E.W., 1970, *JQSRT* 10, 1011
- Vidal C.R., Cooper J., Smith E.W., 1974, *ApJS* 25, 37
- Vrancken M., Hensberge H., David M., Verschueren W., 1997, *A&A* 320, 878
- Wilson R.E., 1979, *ApJ* 234, 1054
- Wilson R.E., 1992, *Documentation of Eclipsing Binary Computer Model*. University of Florida, Gainesville
- Wilson R.E., 1993, In: Leung K.C., Nha I.-S. (eds.) *New Frontiers in Interacting Binary Star Research*. ASP Conf. Ser. 38, p. 91
- Wilson R.E., Biermann P., 1976, *A&A* 48, 349
- Wilson R.E., Devinney E.J., 1971, *ApJ* 166, 605
- Zahn J.P., 1975, *A&A* 41, 329
- Zahn J.P., 1992, In: Duquennoy A., Mayor M. (eds.) *Binaries as tracers of stellar formation*. Cambridge University Press, p. 253